1 **SARS-CoV-2 hijacks neutralizing dimeric IgA for enhanced nasal infection**

2 **and injury**

3

4 Biao Zhou[1,2,11], Runhong Zhou[1,2,11], Jasper Fuk-Woo Chan[2,3,4,5,11], Jianwei Zeng[6,11], Qi

5 Zhang[7,11], Shuofeng Yuan[2,3,4,11], Li Liu[1,2,11], Rémy Robinot[8,11], Sisi Shan[7], Jiwan Ge[6], Hugo

6 Yat-Hei Kwong[1], Dongyan Zhou[1,2], Haoran Xu[1,2], Chris Chung-Sing Chan[2,3], Vincent Kwok-

7 Man Poon[2,3], Hin Chu[2,3,4], Ming Yue[9], Ka-Yi Kwan[1], Chun-Yin Chan[1], Na Liu[1], Chris Chun-

8 Yiu Chan[2,3], Kenn Ka-Heng Chik[2,3], Zhenglong Du[1], Ka-Kit Au[1], Haode Huang[1], Hiu-On

9 Man[1], Jianli Cao[2,3], Cun Li[2,3], Ziyi Wang[6], Jie Zhou[2,3,4], Youqiang Song[9], Man-Lung

10 Yeung[2,3,4], Kelvin Kai-Wang To[2,3,4], David D. Ho[10], Lisa A. Chakrabarti[8], Xinquan Wang[6],

11 Linqi Zhang[7]*, Kwok-Yung Yuen[2,3,4,5]* and Zhiwei Chen[1,2,3,4,12]*

12

13 **Affiliations:**

14 [1]AIDS Institute, Li Ka Shing Faculty of Medicine, the University of Hong Kong, Pokfulam,

15 Hong Kong Special Administrative Region (SAR), China

16 [2]Department of Microbiology, Li Ka Shing Faculty of Medicine, The University of Hong

17 Kong, Pokfulam, Hong Kong SAR, China

18 [3]State Key Laboratory of Emerging Infectious Diseases, The University of Hong Kong,

19 Pokfulam, Hong Kong SAR, China

20 [4]Department of Clinical Microbiology and Infection Control, The University of Hong Kong-

21 Shenzhen Hospital, Shenzhen, Guangdong, China

22 [5]Hainan-Medical University-The University of Hong Kong Joint Laboratory of Tropical

23 Infectious Diseases, and Academician Workstation of Hainan Province, Hainan Medical

24 University, Haikou, Hainan, China, and The University of Hong Kong, Pokfulam, Hong

25 Kong SAR, China.

26 [6]The Ministry of Education Key Laboratory of Protein Science, Beijing Advanced Innovation

27 Center for Structural Biology, Beijing Frontier Research Center for Biological Structure,

28 Collaborative Innovation Center for Biotherapy, School of Life Sciences, Tsinghua

29 University, Beijing 100084, China

30 [7]NexVac Research Center, Comprehensive AIDS Research Center, Center for Infectious

31 Diseases, School of Medicine, Tsinghua University, Beijing 100084, China

32   [8] Control of Chronic Viral Infections Group, Virus & Immunity Unit, Institute Pasteur, Paris,

33   France; CNRS UMR 3569, Paris, France

34   [9]School of Biomedical Sciences, The University of Hong Kong, Hong Kong SAR, China

35   [10]Aaron Diamond AIDS Research Center, Columbia University Vagelos College of

36   Physicians and Surgeons, New York, NY10032, USA

37

38   [11]These authors made equal contributions as co-first authors.

39   *Correspondence: zchenai@hku.hk; zhanglinqi@mail.tsinghua.edu.cn; kyyuen@hku.hk

ABSTRACT

Robust severe acute respiratory syndrome coronavirus-2 (SARS-CoV-2) infection in nasal turbinate (NT) accounts for high viral transmissibility, yet whether neutralizing IgA antibodies can control it remains unknown. Here, we evaluated receptor binding domain (RBD)-specific monomeric B8-mIgA1 and B8-mIgA2, and dimeric B8-dIgA1 and B8-dIgA2 against intranasal SARS-CoV-2 challenge in Syrian hamsters. These antibodies exhibited comparably potent neutralization against authentic virus by competing with human angiotensin converting enzyme-2 (ACE2) receptor for RBD binding. While reducing viruses in lungs, pre-exposure intranasal B8-dIgA1 or B8-dIgA2 led to 81-fold more infectious viruses and severer damage in NT than placebo. Virus-bound B8-dIgA1 and B8-dIgA2 could engage CD209 as an alternative receptor for entry into ACE2-negative cells and allowed viral cell-to-cell transmission. Cryo-EM revealed B8 as a class II neutralizing antibody binding trimeric RBDs in 3-up or 2-up/1-down conformation. Therefore, RBD-specific neutralizing dIgA engages an unexpected action for enhanced SARS-CoV-2 nasal infection and injury in Syrian hamsters.

Keywords

SARS-CoV-2; COVID-19; coronavirus; neutralizing antibody; IgG; cryo-EM; mIgA; dIgA; nasal turbinate; antibody-dependent enhancement

59   **INTRODUCTION**

60   Severe acute respiratory syndrome coronavirus 2 (SARS-CoV-2), a member of the

61   *Betacoronavirus* genus, is the causative agent of Coronavirus Disease 2019 (COVID-19) [1].

62   SARS-CoV-2 enters host cells through the binding of the receptor binding domain (RBD) of

63   its surface trimeric spike (S) protein to the cellular angiotensin-converting enzyme-2 (ACE-

64   2) receptor [2-4]. After the ACE2 binding, the S protein is cleaved into S1 and S2 subunits by

65   host cellular proteases including the transmembrane protease serine 2 (TMPRSS2) to

66   promote fusion of viral and cellular membranes for viral entry [5-8]. Apparently, these entry

67   processes are similar to those of SARS-CoV-1 [9-12], the causative agent of SARS, although

68   these two coronaviruses share just 76% and 40% amino acid identity between their genomes

69   and their RBD external subdomains, respectively [13,14]. SARS-CoV-2, however, has displayed

70   remarkably higher transmissibility than SARS-CoV-1. By August 2021, the rapid all-year-

71   round transmission of SARS-CoV-2 has resulted in over 200 million infections and 4 million

72   deaths globally [15] since the outbreak of COVID-19 reported in December 2019. This is in

73   marked contrast to the SARS epidemic, which caused only 8096 cases and 774 deaths, and

74   disappeared in 2003 [16]. Therefore, understanding the mechanisms underlying the high

75   transmissibility of SARS-CoV-2 is essential for pandemic control.

76

77   The high transmissibility of SARS-CoV-2 is likely associated with multiple factors. First,

78   unlike SARS-CoV-1-infected cases characterized by high fever and prominent respiratory

79   symptoms, afebrile individuals with SARS-CoV-2 were often found upon diagnosis, allowing

80   person-to-person transmissions by asymptomatic carriers including international travellers [17-

81   20]. Second, while both coronaviruses employ the same receptor ACE2, highly conserved

82   RBD residues or side chain properties of SARS-CoV-2 might account for increased ACE2

83   binding [9-12]. Third, the unique insertion of the PRRA sequence in SARS-CoV-2 S

84   glycoprotein promotes higher virion infectivity and cell-cell fusion, leading to enhanced

85   pathogenicity *in vivo* [21-23]. Fourth, by altering the S protein conformation, the D614G

86   mutation increases the stability of S trimer to avoid premature S1 shedding, which results in a

87   rapid dominance of this mutation globally [24,25]. The D614G mutation also induces higher

88   infectious titres in nasal washes and the trachea of infected hamsters [26]. Multiple mechanisms,

89   therefore, contribute to the high upper respiratory tract (URT) viral loads characteristic of

90   SARS-CoV-2 infection [27-29], which facilitates viral transmission in the human population. Till

91   now, the role of nasal IgA remains understudied. In particular, whether antibody-dependent

4

92   enhancement (ADE) of SARS-CoV-2 infection has any place *in vivo* remains an open

93   question [30].

94

95   Since the outbreak of COVID-19, worldwide research efforts have led to the identification of

96   many potent human neutralizing antibodies (HuNAbs) mainly in IgG form for preclinical and

97   clinical developments [31-38]. Some studies also investigated IgA antibodies, which are known

98   to play an important role in mucosal immunity, especially in their secretory form (SIgA) [39,40].

99   RBD-specific IgA antibodies were rapidly discovered in COVID-19 patients [41]. IgA and

100   SIgA were even shown to dominate the early antibody response as compared to IgG and IgM

101   in saliva and bronchoalveolar lavage fluids due to expansion of IgA plasmablasts with

102   mucosal homing characteristics [42,43]. However, it was noted that COVID-19 patients with

103   acute respiratory distress syndrome (ARDS) had higher SIgA in the airway mucosa for

104   unknown reasons [44]. Moreover, a recent study reported that SARS-CoV-2 viral loads were

105   closely associated with spike-specific IgA responses in the nasal samples of acute COVID-19

106   patients [45]. Since dIgA were shown to be about 15 times more potent than mIgA *in vitro*

107   against the same target, dIgA were suggested to be particularly valuable for therapeutic

108   application against SARS-CoV-2 [46]. It is essential to investigate the potential of mIgA and

109   dIgA in preventing SARS-CoV-2 infection *in vivo*.

110

111   In this study, we used the technology of single B cell antibody gene cloning to generate a

112   panel of SARS-CoV-2 RBD-specific monoclonal HuNAbs from the peripheral blood

113   mononuclear cells (PBMCs) of one acute and three convalescent COVID-19 patients in Hong

114   Kong. Since intramuscular or intranasal inoculation of several potent IgG HuNAbs cannot

115   completely prevent SARS-CoV-2 infection in the nasal turbinate (NT) of Syrian hamsters [47],

116   we sought to improve the efficacy of HuNAb by converting IgG to IgA. To achieve this goal,

117   we engineered the potent B8-IgG1 into monomeric IgA1 (B8-mIgA1), monomeric IgA2 (B8-

118   mIgA2), dimeric (B8-dIgA1) and dimeric IgA2 (B8-dIgA2), and determined their efficacies

119   in the Syrian hamster model against the live intranasal SARS-CoV-2 challenge [48].

120

121   **RESULTS**

122   **Characterization of human monoclonal antibodies from COVID-19 patients**

123   To isolate human monoclonal antibodies (MAbs), we obtained peripheral blood mononuclear

124   cells (PBMCs) from one acute (P4) and three convalescent (P1-P3) COVID-19 patients in

125   Hong Kong at a mean 73.5 ($\pm$25) days after symptoms onset (Supplementary Table 1).

126   Enzyme-linked immunosorbent assay (ELISA) and pseudovirus neutralization assays

127   revealed that all patient sera showed SARS-CoV-2 RBD- and spike-specific binding (Fig. 1A

128   and 1B) and neutralizing antibody (NAb) activities (Fig. 1C). The mean NAb IC_{50} titer was

129   1:1753 with a range of 1:638-1:5701. Flow cytometry was then used to sort SARS-CoV-2-

130   specific immunoglobulin positive (IgG^+) memory B cells from individual PBMC samples

131   using two fluorescent-conjugated RBD probes. The percentage of RBD-binding IgG^+

132   memory B cells ranged from 0.19% to 0.52% (Supplementary Fig. 1A and Supplementary

133   Fig. 1B). We successfully cloned a total of 34 MAbs from these patients, including 3 from

134   P1, 8 from P2, 17 from P3 and 6 from P4. We confirmed that 18 of these MAbs exhibited

135   RBD-specific binding activities detected by ELISA (Supplementary Fig. 1C). No clear

136   dominance of heavy (H) chain gene family was found among these 4 subjects by sequence

137   analysis (Fig. 1D, left panels). VLK1, however, was the most used variable gene family for

138   the light (L) chain (Fig. 1D, right panels). The average somatic hypermutation (SHM) rate

139   ranged from 0% to 12.2% for the H chain and from 0.7% to 7.9% for the L chain (Fig. 1E,

140   left). The average complementarity-determining region 3 (CDR3) lengths ranged from 12.3

141   to 17.4 for the H chain and 8.4 to 9.4 for the L chain, respectively (Fig. 1E, right). These

142   results suggested overall comparable degrees of affinity maturation in these RBD-specific

143   human MAbs obtained from individual memory B cells of four Hong Kong patients.

144

145   **Specificity and potency of SARS-CoV-2-specific human neutralizing antibodies**

146   To determine the antiviral activities of these 18 RBD-specific human MAbs, we performed

147   binding and neutralization assays. Five of them, namely A6-IgG1, B4-IgG1, B7-IgG1, B8-

148   IgG1 and C5-IgG1 displayed RBD- and spike- specific binding by ELISA (Fig. 1F) and

149   neutralizing activities against both pseudotyped and authentic viruses (Fig. 1G and

150   Supplementary Fig. 1D). Interestingly, the four most potent HuNAbs, B4-IgG1, B7-IgG1,

151   B8-IgG1 and C5-IgG1, all came from patient P3 (Supplementary Fig. 1D). Sequence

152   analysis revealed strong similarities between B7-, B8-, and C5-IgG1, which all contained an

153   IGHV1-69 heavy chain gene and an IGKV3 kappa light chain gene. B4-IgG1 contained

154   distinct IGHV3-66 and IGKV1-33 genes with CDR3 lengths of 12 amino acids (aa) and 9 aa,

155   and somatic hypermutation (SHM) rate of 3.8% and 4.6%, respectively (Supplementary

6

156   Table 2). B7 and B8 were the most similar, as both contained IGHV1-69 and IGKV3-11

157   though B8 had a shorter CDR3 (14 aa vs 18 aa) and higher SHM (4.8% vs 0.0%) than those

158   of B7 in the heavy chain. In the L chain, B7 and B8 shared a 9 aa CDR3, but B8 had a higher

159   SHM rate than that of B7 (1.7% vs 0.7%) C5-IgG1 had a similar IGHV1-69 light chain gene

160   with a 16 aa CDR3 and 2.4% SHM, but a different IGKV3-20 with a 9 aa CDR3 and 2.8%

161   SHM.   By ELISA, these four P3-derived HuNAbs bound to the SARS-CoV-2 RBD with

162   half-maximal effective concentration (EC_{50}) values ranging from 0.02 to 0.06 µg/ml,

163   indicating stronger binding than that of the P4-derived A6-IgG1 (0.3 µg/ml) (Fig. 1F, left and

164   Supplementary Table 3). P3-derived MAbs also exhibited stronger binding activities to the

165   spike, with the EC_{50} values ranging from 0.018 to 0.06 µg/ml, compared to A6-IgG1 (17.94

166   µg/ml) (Fig. 1F, right and Supplementary Table 3). Neutralizing assays using pseudoviruses

167   revealed that these four potent HuNAbs had IC_{50} values ranging from 0.0095 to 0.038 µg/ml,

168   and IC_{90} values ranging from 0.046 to 0.136 µg/ml, respectively (Fig. 1G, left and

169   Supplementary Table 4). Moreover, B8 proved to be the most potent HuNAb, capable of

170   inhibiting authentic SARS-CoV-2 with an IC_{50} value of 0.013 µg/ml and an IC_{90} value of

171   0.032 µg/ml, respectively (Fig. 1G, right and Supplementary Table 4). We then determined if

172   these HuNAbs could compete with ACE2 for RBD binding by surface plasmon resonance

173   (SPR). We found that all of them strongly competed with ACE2 (Fig. 1H). In line with the

174   ELISA results, B8-IgG1 displayed the best KD value for RBD binding (169 pM)

175   (Supplementary Fig. 2A, Supplementary Table 5) and the strongest competition with ACE2

176   (Fig. 1H), which explained its potent neutralizing activity. As B4-IgG1 displayed only partial

177   competition for RBD binding with the other antibodies (Supplementary Fig. 2B), we further

178   performed antibody synergy experiments using the pseudotype neuralization assay. No

179   significant synergistic effects were found between any pairs of these four HuNAbs

180   (Supplementary Fig. 2C). These results demonstrated that B4-, B7-, B8- and C5-IgG1 were

181   all RBD-specific and competed with ACE2 for similar sites on the RBD.

182

183   **B8-IgG1 pre-exposure prophylaxis and post-exposure treatment in the golden Syrian**

184   **hamster model**

185   To determine the efficiency of B8-IgG1 in pre-exposure prophylaxis and post-exposure

186   treatment against live intranasal SARS-CoV-2 infection, we administered B8-IgG1

187   intraperitoneally in golden Syrian hamsters, before or after viral challenge in our Biosafety

188   Level-3 (BSL-3) animal laboratory (Fig. 2A). In the pre-exposure prophylaxis group (G1, n

7

189   = 4), each hamster received a single intraperitoneal injection of 1.5 mg/kg B8-IgG1. In the

190   post-exposure treatment groups, each hamster received a single intraperitoneal injection of

191   1.5 mg/kg B8-IgG1 at day 1 (G2, n = 4), day 2 (G3, n = 4) or day 3 (G4, n = 4) postinfection

192   (dpi), respectively (Fig. 2A). The challenge dose was 10^5 plaque-forming units (PFU) of live

193   SARS-CoV-2 (HKU-001a strain) [47,48]. Another group of hamsters (G0, n = 4) received PBS

194   injection as a no-treatment control. One G4 animal died accidentally during the procedure.

195   Since Syrian hamsters recover quickly from SARS-CoV-2 infection, with resolution of

196   clinical signs and clearance of virus shedding within one week after infection [26,48], we chose

197   to sacrifice the animals at 4 dpi for HuNAb efficacy analysis, at a time when high viral loads

198   and acute lung injury were consistently observed. At 4 dpi, NT and lung tissues were

199   harvested to quantify infectious viruses by measuring PFUs, viral RNA loads by real-time

200   reverse-transcription polymerase chain reaction (RT-PCR) and infected cells by

201   immunofluorescence (IF) staining of viral nucleocapsid protein (NP)-positive cells as we

202   described previously [47,48].

203

204   We found that infectious virus, measured by PFU, weas readily detected in all tissue

205   compartments of G0 hamsters but not in the lungs of 75% G1, 100% G2, 75% G3 and 0% G4

206   animals, nor in the NT of 50% G1, 75% G2, 50% G3 and 25% G4 animals (Fig. 2B and 2E).

207   The decrease in PFU was of 2-3 orders of magnitude, suggesting efficient viral suppression in

208   the lungs for the G1, G2, and G3 groups. A sensitive RT-PCR assay further demonstrated that

209   viral RNA copy numbers were decreased in the lungs by 3 orders of magnitude in 50% of G1

210   hamsters (Fig. 2C). In contrast, there was no significant viral RNA reduction in the NT of G1

211   animals (Fig. 2F), suggesting lower efficacy of B8-IgG1 to prevent viral entry in the URT

212   than in the lungs. There were slight but not significant viral RNA load decreases in both

213   lungs and NT of G2 and some G3 animals. We then evaluated the number of infected cells or

214   foci in these two tissue compartments by anti-NP antibody staining. A clear decrease of NP-

215   positive cells or foci was observed in the lungs of G1 and G2 hamsters (Fig. 2D). Abundant

216   NP-positive cells with a diffuse distribution, however, were readily detected in the NT of all

217   the challenged hamsters (Fig. 2G). These results demonstrated that systemic B8-IgG1

218   injection was effective at reducing productive SARS-CoV-2 infection in the lungs when used

219   for pre-exposure prophylaxis and early treatment especially within 48 hours post infection,

220   but was insufficient to prevent viral infection in the NT.

221

222　　To determine the correlates of B8-IgG1-mediated protection, we also measured the antibody
223　　concentration in serum, lung homogenate and NT homogenates at 0 and 4 dpi for all
224　　experimental animals. On average, 4,257 ng/ml and 2,101 ng/ml B8-IgG1 were found in
225　　animal sera at 0 and 4 dpi (Supplementary Table 6). On 4 dpi, lung and NT homogenates
226　　contained 128 ng/ml and 20 ng/ml in G1, 238 ng/ml and 86 ng/ml in G2, 229 ng/ml and 93
227　　ng/ml in G3, and 192 ng/ml and 46 ng/ml in G4 animals, respectively. These results
228　　demonstrated that most animals maintained higher peripheral B8-IgG1 antibody
229　　concentration, while a decreasing concentration gradient was observed in the lungs and NT
230　　during infection. The concentrations of B8-IgG1 measured in NT homogenates were close to
231　　the neutralization IC_{90} measured *in vitro* (32 ng/ml), explaining why infectious virus was
232　　undetectable in the PFU assay. These findings are in line with results obtained for other
233　　potent IgG HuNAbs administered systemically, as reported in our previous study [47]. The B8-
234　　IgG1 concentrations measured in the NT appeared insufficient to completely block infection
235　　*in vivo*, as indicated by the presence of NP-positive cells scattered throughout the NT.

236

237　　Pre-exposure prophylaxis by monomeric B8-mIgA1 and B8-mIgA2 in Syrian hamsters

238　　Since systemic administration of the RBD-specific neutralizing B8-IgG1 did not suppress
239　　SARS-CoV-2 nasal infection effectively, we sought to construct various types of IgA for
240　　mucosal intervention. For this purpose, we engineered B8-IgG1 into monomeric B8-mIgA1
241　　and B8-mIgA2, and then into dimeric B8-dIgA1 and B8-dIgA2 by introducing the J chain.
242　　By *in vitro* characterization, purified B8-mIgA1, B8-mIgA2, B8-dIgA1 and B8-dIgA2
243　　retained similar binding to RBD and spike by ELISA as compared to B8-IgG1
244　　(Supplementary Fig. 3A-B, Supplementary Table 7), and comparable antiviral activities
245　　based on neutralization IC_{50} and IC_{90} values ((Supplementary Fig. 3C-D and Supplementary
246　　Table 8). That said, B8-mIgA2 and B8-dIgA2 showed slightly more potent IC_{90} activities
247　　than B8-IgG1 in the pseudovirus neutralization assay using 293T-ACE2 cells as targets
248　　(Supplementary Table 8). After introducing J chain, the proper dimer formation of B8-dIgA1
249　　and B8-dIgA2 was confirmed by size exclusion chromatography analysis (Supplementary Fig.
250　　3E-F).   Furthermore, B8-mIgA1, B8-mIgA2, B8-dIgA1 and B8-dIgA2 also retained
251　　comparable competition with ACE2 for binding to spike by SPR analysis (Supplementary Fig.
252　　3G-J). Therefore, the engineered IgA had the expected structural properties, and showed
253　　antiviral activities as potent as those of B8-IgG1 *in vitro*.

254   We then evaluated the monomeric B8-mIgA1 and B8-mIgA2 in the hamster model, using a

255   higher 4.5 mg/kg dose via either intranasal or intraperitoneal injection, and used the same

256   amount of intranasal B8-IgG1 inoculation as a control (Fig. 3A to 3I). Interestingly, while

257   changes in total RdRp and subgenomic sgNP viral RNA loads were not obvious (Fig. 3D to

258   3E), B8-IgG1 and B8-mIgA1 (both *i.n.* and *i.p.*), but not B8-mIgA2, were able to

259   significantly suppress infectious virus production (PFU) in the lungs of 75% infected

260   hamsters by 2 orders of magnitude (Fig. 3D). Sporadic infected cell foci were still detected in

261   the lung sections by anti-NP staining (Fig. 4E and Supplementary Fig. 4A), suggesting that

262   protection conferred by B8-IgG1 and B8-mIgA1 was not complete. B8-mIgA2 was not able

263   to suppress viral RNA load nor PFU in the challenged hamsters, regardless of the route of

264   antibody injection. On the other hand, like B8-IgG1, both B8-mIgA1 and B8-mIgA2 did not

265   achieve significant viral suppression in the NT. After intranasal administration of either B8-

266   mIgA1 or B8-mIgA2, some hamsters even showed a trend of slightly increased infectious

267   virus production in NT, though this did not reach statistical significance (Fig. 3F-3H). Among

268   these animals, the NP-positive cells were detected readily in the NT, as demonstrated by the

269   whole section scanning, indicating the comparable distribution compared with the B8-IgG1

270   and no-treatment groups (Fig. 3I). These results were consistent with many NP-positive cells

271   observed in diffusely infected areas of NT by classic IF (Supplementary Fig. 4B). These

272   results demonstrated that B8-mIgA1 was more potent than B8-mIgA2 at limiting SARS-

273   CoV-2 infection in the lungs, but that both mIgA did not prevent nor significantly limit

274   SARS-CoV-2 nasal infection.

275

276   **B8-dIgA1 and B8-dIgA2 mediate enhancement of SARS-CoV-2 nasal infection and**

277   **injury in Syrian hamsters**

278   Next, we tested the effects of dimeric B8-dIgA1 and B8-dIgA2 in Syrian hamsters. To

279   improve protective efficacy of intranasal dIgA treatment, we included a 3-fold higher dosage

280   group of 13.5 mg/kg besides the 4.5 mg/kg group (Fig. 4A to 4I), and we shortened the

281   interval between dIgA and virus inoculation to 12 hours (Fig. 4A). Both RdRp and sgNP viral

282   RNA loads dropped significantly in the lungs of hamsters that received the high dose of B8-

283   dIgA2 compared to the no-treatment group (Fig. 4B and 4C). Both B8-dIgA1 and B8-dIgA2

284   at the high dose also suppressed infectious viruses (PFU) in the lungs of 75% and 100%

285   treated hamsters, respectively (Fig. 4D). High dose B8-dIgA1 and B8-dIgA2 also decreased

286   the number of NP-positive cells or foci in the lungs, with a more marked change for B8-

287   dIgA2 (Fig. 4E and Supplementary Fig. 5A).   Unexpectedly, however, we observed

288   significantly enhanced SARS-CoV-2 nasal infection and tissue damage in most infected

289   hamsters included the low and high dose groups of both B8-dIgA1 and B8-dIgA2, in all the

290   four assays used (Fig. 4F to 4I). High dose administration of B8-dIgA1 or B8-dIgA2 resulted

291   in increased PFU production in the NT by 37-fold and 81-fold, respectively, compared to the

292   no-treatment group (Fig. 4H). Since our model showed comparable NT PFU on day 2 and

293   day 4 as described previously [48], this level of enhanced infection was unusual. It was also not

294   observed with B8-IgG1 or monomeric B8-mIgA1 and B8-mIgA2 treatment, as described

295   above. Moreover, the distribution of NP-positive cells in hamsters treated with dimeric B8-

296   IgA was broader and reached deeper into NT tissue compared to the no-treatment group, as

297   shown by whole section scanning (Fig. 4I and Supplementary Fig. 5B), which was associated

298   with more severe and extensive epithelium desquamation and luminal cell debris

299   (Supplementary Fig. 5C). The density of nasal NP^+ cells was also significantly higher in B8-

300   dIgA2-treated hamsters than in PBS-treated animals (Supplementary Fig. 5D-E). It is

301   therefore conceivable that treatment with dimeric B8-IgA expanded the type and distribution

302   of target cells in the nasal epithelium. Critically, we confirmed that control dimeric dIgA1

303   and dIgA2 did not enhance SARS-CoV-2 infection under the same experimental conditions

304   (Supplementary Fig. 6). These results demonstrated that, instead of inducing viral

305   suppression, pre-exposure dimeric B8-dIgA1 and B8-dIgA2 enhanced SARS-CoV-2 nasal

306   infection and injury significantly in Syrian hamsters, which was consistently found in three

307   independent experiments.

308   To validate the role of B8-dIgA1 and B8-dIgA2, we then measured B8-IgA concentrations in

309   the serum at day 0 and 4 dpi, and in the lung and NT homogenates at 4 dpi. B8-dIgA1 and

310   B8-dIgA2 were primarily detected in lung homogenates at 4 dpi and were apparently

311   undetectable in the serum and NT homogenates (Supplementary Table 9). The enhanced

312   viral replication in NT probably exhausted B8-dIgA1 and B8-dIgA2 locally, through

313   antibody-virus complex formation and clearance [30]. To address this possibility, we treated

314   separately five groups of naïve Syrian hamsters (n=4 per group) with each antibody at the 4.5

315   mg/kg dose. Twelve hours after the inoculation, antibody concentrations were readily

316   detected in each tissues compartment (Supplementary Table 10). The highest concentrations

317   of dIgA antibodies were found in lung homogenates, followed by nasal washes, NT

318   homogenates, and serum. These results suggest that B8-dIgA1 and B8-dIgA2 concentrations

319   in the NT and lungs were still above their neutralization IC_{90} values at the time of viral

320   challenge, indicating that the results obtained in our experiments could not be explained by

321   the insufficient amounts of antibodies.

322

B8-dIgA1- and B8-dIgA2-mediated enhancement of SARS-CoV-2 infection via CD209

324   Since B8 antibodies share the same binding site to the RBD domain, we sought to investigate

325   possible mechanisms of B8-dIgA1- and B8-dIgA2-enhanced infection. First, we consistently

326   found that 10 ng/ml B8-dIgA1 or B8-dIgA2 completely neutralized SARS-CoV-2 infection

327   in human renal proximal tubule cells (HK-2), as measured in our previously reported

328   immunofluorescence assay (Supplementary Fig. 7) [49]. We also tested B8-mIgA2 and B8-

329   dIgA2 neutralizing capacity in the MucilAir[TM] model, consisting of a reconstructed human

330   nasal epithelium, which contained goblet, ciliated, and basal cells (Fig. 5A) [50]. Both B8-

331   mIgA2 and B8-dIgA2 neutralized SARS-CoV-2 in a dose-dependent fashion, when

332   compared to a dIgA2 control antibody. Similar experiments were carried out in the presence

333   of the mucus naturally secreted by goblet cells, to determine whether dIgA interaction with

334   the mucus may alter their neutralization capacity. However, B8-dIgA2 showed the same

335   neutralization capacity in the presence and absence of mucus. These results demonstrated that

336   B8-dIgA1 and B8-dIgA2 did not enhance SARS-CoV-2 infection in either human HK-2 or

337   primary airway epithelial cells, which primarily expressed human ACE2 as a viral receptor.

338   We then turned our attention to ACE2-independent mechanisms that might be associated with

339   dimeric IgA-mediated enhancement of SARS-CoV-2 infection. Considering that mucosal

340   monocyte-derived dendritic cells (DC) could mediate SARS-CoV-1 infection and

341   dissemination in rhesus monkeys as early as 2 dpi, as we previously reported [51], we sought to

342   investigate the role of DC-expressed surface receptors. We focused on CD209 (DC-SIGN),

343   because this lectin was previously shown to act as a cellular receptor for secretory IgA [52]. By

344   IF staining, intranasal administration of B8-dIgA2 alone did not increase CD209 expression

345   in the NT of treated hamsters (Fig. 5B, left). Upon SARS-CoV-2 infection, however, we

346   noted an increase in CD209-positive cells in olfactory epithelium devoid of ACE2 expression

347   (Fig. 5B, middle). Importantly, most CD209^{+} cells were positive for NP (Fig. 5B, right),

348   indicating that these CD209^{+} cells were likely permissive to SARS-CoV-2 infection. We then

349   determined whether B8-dIgA1 and B8-dIgA2 could enhance SARS-CoV-2 infection in 293T

350   cells expressing human CD209 or CD299 but not ACE2. Using a low MOI of 0.05, we found

351   that pre-incubation of B8-dIgA1 and B8-dIgA2 enhanced live SARS-CoV-2 infection

352   significantly in 293T cells expressing human CD209, as determined by increased viral NP

12

353   production (Fig. 5C). Interestingly, human CD299, a type II integral membrane protein that

354   is 77% identical to CD209, did not show similar activities in the same experiment (Fig. 5C).

355   Control dIgA1 and dIgA2 did not show any enhancement in NP^+ cell detection compared

356   with virus only. Considering that $CD209^+$ DCs promote HIV-1 transmission to $CD4^+$ T cells

357   via cell-cell contacts, we speculated that B8-dIgA1 and B8-dIgA2 might not be able to block

358   the similar process for SARS-CoV-2. Indeed, by testing the B8 antibodies at concentrations

359   100-times higher than IC_{90} neutralization values (around 3000 ng/ml), none of B8-IgG1, B8-

360   mIgA1, B8-mIgA2, B8-dIgA1 and B8-dIgA2 could block cell-cell fusion (Fig. 5D). Taken

361   together, our results demonstrated that B8-dIgA1- and B8-dIgA2-enhanced SARS-CoV-2

362   nasal infection likely involved viral capture and infection of mucosal $CD209^+$ cells, followed

363   by more robust infection of $ACE2^+$ epithelial cells through trans-infection via cell-cell spread

364   in NT.

365

Cryo-EM analysis of the spike-B8 complex

367   To understand the potential mechanism of action of B8 HuNAb, we performed a cryo-EM

368   single-particle analysis of B8 Fab bound to the SARS-CoV-2 spike ectodomain trimer

369   (Supplementary Fig. 8). Two B8-spike complex structures were determined based on 351,095

370   and 616,799 particles collected, respectively (Supplementary Table 11). One structure at 2.67

371   Å resolution contained the spike with all three RBDs adopting the "up" conformation (3u),

372   where each "up" RBD was bound by one B8 Fab (Fig. 6A-B). The other structure at 2.65 Å

373   resolution contained one spike trimer with 2 RBDs in the "up" conformation and 1 RBD in

374   the "down" conformation (2u1d), where each RBD was also bound by one B8 Fab despite the

375   presence of two distinct RBD conformations (Fig. 6C-D). After superimposing the "3u" and

376   "2u1d" spikes, a ~53-degree rotation was observed between the "up" RBD (red color) in the

377   3u spike trimer and the "down" RBD (gray) in the 2u1d spike trimer (Fig. 6E). The B8 Fab

378   appeared to bind to the receptor-binding motif (RBM) of the RBD through its heavy chain for

379   most of the interactions (Fig. 6F-G). Therefore, the cellular receptor ACE2 would clash with

380   the B8 Fab due to the overlap of their respective epitopes on the RBM (Fig. 6F-H and

381   Supplementary Table 12). The elucidation of the epitope revealed that B8 could be grouped

382   into the SARS-CoV-2 neutralizing antibody class II [53]. These structural findings were further

383   supported by neutralization assays using a panel of pseudoviruses containing naturally

384   occurring mutations. Indeed, the E484K mutation from the South African SA□9 strain,

385   which is located within the B8-binding interface, caused a major loss of neutralizing potency

386 for all the B8 isotypes tested: IgG1, mIgA1, mIgA2, dIgA1 and dIgA2 (Supplementary Table

387 13). The comparable neutralization profiles of these NAbs against the full panel of viral

388 variants also indicated that the conformation of key RBD-binding residues remained

389 unchanged after engineering of the constant regions of these B8 isotypes.

390

391 **DISCUSSION**

392 In this study, we investigated the preventive potential of a potent RBD-specific NAb B8

393 primarily in the forms of monomeric and dimeric IgA against live intranasal SARS-CoV-2

394 infection in the golden Syrian hamster model as compared with B8-IgG1 [47,48]. While these

395 B8-IgA antibodies maintained neutralizing activities against SARS-CoV-2 *in vitro* similar to

396 those of B8-IgG1, they displayed distinct *in vivo* effects, with clear differences in their

397 capacity to modulate viral infection in the NT. Pretreatment by intranasal administration of

398 4.5 mg/kg of monomeric B8-mIgA1 or B8-mIgA2 did not significantly reduce infectious

399 virus production in the NT homogenates. On the contrary, the antibody isotype had a marked

400 effect, as intranasal administration of 4.5 mg/kg and 13.5 mg/kg dimeric B8-dIgA1 or B8-

401 dIgA2 paradoxically increased the amount of infectious virus (PFU) in NT homogenates.

402 This enhancing effect was not observed with several intranasal IgG HuNAbs previously

403 tested by other groups or our team [47,54]. Mechanistically, instead of neutralization, virus-

404 bound B8-dIgA1 and B8-dIgA2 used CD209 as an alternative receptor to infect non-ACE2

405 cells. CD209$^+$ cells were increased and permissive to viral infection in the olfactory

406 epithelium of Syrian hamsters upon SARS-CoV-2 infection, suggesting that this cell

407 population could contribute to viral mucosal seeding. Indeed, we found that CD209

408 expressing cells could be infected *in vitro* by live SARS-CoV-2 at 0.05 MOI in the presence

409 of B8-dIgA1 and B8-dIgA2. Since none of the B8-based MAbs could prevent SARS-CoV-2

410 cell-to-cell transmission, even at high concentration *in vitro*, virus-laden mucosal CD209$^+$

411 cells might trans-infect ACE2$^+$ cells through cell-to-cell contacts in NT, resulting in enhanced

412 infection and injury. Cryo-EM analysis further indicated that B8 is a typical class II HuNAb

413 that binds to the SRAS-CoV-2 spike RBD in either a 3u or a 2u1d mode. Our findings,

414 therefore, reveal a previously unrecognized pathway for RBD-specific dimeric IgA-mediated

415 enhancement of SARS-CoV-2 nasal infection and injury in Syrian hamsters.

416

417 The role of dimeric IgA has been explored primarily for mucosal transmitted viruses. At the

418 mucosal surface, the major IgA type is the secretory form, which is generated from dIgA by

14

419　the acquisition of a secretory component upon endocytosis and secretion by epithelial cells.
420　In the simian AIDS macaque model, neutralizing dIgA given directly into the rectal lumen
421　can prevent viral acquisition in rhesus monkeys challenged via the mucosal route [55].
422　Although the administered dIgA did not contain the secretory component (SC), they might
423　have associated with free SC, which is present in mucosal secretions such as human lung
424　lavages [56]. Neutralizing dIgA1 and dIgA2 could be protective through several mechanisms,
425　including direct virus neutralization, virion capture, or the inhibition of virion transcytosis
426　across the epithelium [40]. In this macaque study, however, Watkins et al. demonstrated that the
427　dimeric HGN194 dIgA2 protected only 1/6 animals in a rectal challenge model [55]. Recently,
428　Taylor et al. found an increase in virion number and penetration depth in the transverse colon
429　and mesenteric lymph nodes, after mucosal treatment with the HGN194 dIgA2 compared to
430　a PBS control [57]. The authors suggested that virus-specific dIgA somehow mediated the
431　delivery of virus immune complexes to the mesenteric lymph nodes for systemic infection.
432　Here, we report that SARS-CoV-2 may subvert the action of potent neutralizing antibodies,
433　as pretreatment with neutralizing B8-dIgA1 and B8-dIgA2 induced a more robust nasal
434　infection via a previously unrecognized mode of viral enhancement.

435

436　SARS-CoV-2 engages CD209$^+$ cells to evade ACE2-dependent neutralizing B8-dIgA1 and
437　B8-dIgA2 for enhanced NT infection and injury. Previous studies have indicated various
438　scenarios for ADE occurrence in viral infections. The well-known dengue ADE has been
439　associated with poorly neutralizing cross-reactive antibodies against a heterologous viral
440　serotype, leading to increased infection of FcγR-expressing cells [58]. Recent findings
441　suggested that an increase in afucosylated antibodies contribute to dengue ADE [59]. In
442　contrast, vaccine-associated enhanced respiratory disease induced by respiratory syncytial
443　virus has not been found to be antibody-dependent [60]. For SARS and MERS, ADE observed
444　*in vitro* depended on binding of the antibody Fab to the virus and the binding of the Fc
445　component to FcγR on target cells [61]. One study found that spike IgG antibody abrogated
446　wound-healing responses in SARS-CoV-1-infected Chinese macaques [62]. In the case of
447　COVID-19, vaccination and passive immunization studies have not revealed ADE of disease
448　severity [63]. Comprehensive studies, however, are necessary to define the clinical correlates of
449　protective immunity against SARS-CoV-2, especially in the context of vaccine breakthrough
450　infections. During natural infection, one study indicated that the increase in afucosylated
451　antibodies might contribute to COVID-19 severity [64]. To date, four classes of potent HuNAbs
452　have been isolated from convalescent COVID-19 patients [34,53]. The molecular mechanism of

453   neutralization for most potent HuNAbs was primarily through blocking the interaction
454   between ACE2 and the spike RBD. Currently, systemic RBD-specific HuNAb treatment
455   remains to be improved for therapeutic suppression of SARS-CoV-2 replication in the NT or
456   URT, both in animal models and human trials [47,48,65]. One limitation is the insufficient
457   amounts of HuNAbs distributed on the nasal mucosal surface for protection [47]. Other reasons
458   might include alternative entry pathways engaged by SARS-CoV-2 to evade HuNAbs. To
459   this end, Liu et al. reported recently that antibodies against the spike N-terminal domain
460   (NTD) induced an open conformation of the RBD and thus enhanced the binding capacity of
461   the spike to the ACE2 receptor, leading to increased viral infectivity [66]. Yeung et al.
462   demonstrated nicely that SARS-CoV-2 could engage soluble ACE2 (sACE2) and then bind
463   alternate receptors for viral entry, through interaction between a spike/sACE2 complex with
464   the angiotensin II AT1 receptor, or interaction between a spike/sACE2/vasopressin complex
465   with the AVPR1B vasopressin receptor, respectively [49]. In this study, we found that, in the
466   presence of potent neutralizing B8-dIgA1 or B8-dIgA2 antibodies, SARS-CoV-2 used the
467   cellular receptor CD209 for capture or infection, which likely expanded the use of CD209$^+$
468   cells as target cells, leading to enhanced NT infection and trans-infection. Interestingly, a
469   preprint report suggests that cells expressing CD209 can be infected directly by SARS-CoV-2
470   through an interaction of the spike with the NTD instead of the RBD [67]. This mode of action,
471   however, was unlikely to explain our findings, because no enhancement of SARS-CoV-2
472   nasal infection was found in presence of control dIgA1 and dIgA2. Our results rather suggest
473   that the direct binding of virus-bound B8-dIgA1 or virus-bound B8-dIgA2 to CD209 is a
474   likely pathway, resulting in the more severe SARS-CoV-2 nasal infection and damage. In
475   line with our results, a previous study demonstrated that dIgA itself can use CD209 as a
476   cellular receptor [52]. During the entry process, since neither B8-dIgA1 nor B8-dIgA2 could
477   prevent virus cell-to-cell transmission, infected mucosal CD209$^+$ cells might enable a more
478   robust viral transmission to ciliated nasal epithelial cells in NT, which show the highest
479   expression of ACE2 and TMPRSS2 receptors [65]. In support of this notion, previous studies
480   indicated that mucosal DCs can capture HIV-1 through binding of its envelope glycoproteins
481   to CD209 and efficiently transfer the bound virions to CD4$^+$ T cells, in a process called trans-
482   enhancement or trans-infection [68]. The trans-infection markedly decreased the neutralization
483   efficiency of potent NAbs directed at HIV [69]. Moreover, although monocyte-derived DCs
484   (MDDCs) cannot support productive SARS-CoV-2 replication [70], a recent study
485   demonstrated that MDDCs could mediate efficient viral trans-infection of the Calu-3 human
486   respiratory cell line [71]. Our findings of increased number of infectious viruses in NT,

16

487 therefore, have significant implications for SARS-CoV-2 transmission, COVID-19
488 pathogenesis, and immune interventions.

489

490 **Limitations of the study**

491 As our *in vivo* findings were obtained in Syrian hamsters, it remains to be determined
492 whether CD209+ DCs are abundantly recruited to the nasal mucosa in SARS-CoV-2-infected
493 humans. It is, however, known that myeloid DCs are increased in the nasal epithelium upon
494 infection [51,72]. Our preliminary analysis of the human nasal cytology data (under accession
495 code EGAS00001004082) revealed the presence of increased CD209+ DCs in addition to
496 abundant ACE2, TMPRSS2, and furin expression in the apical side of multiciliated cells of
497 SARS-CoV-2-infected human subjects (Supplementary Fig. 9) [73]. Another limitation is that
498 we did not have an NTD-specific neutralizing dIgA for comparison. Besides the class II
499 neutralizing dIgA such as B8-mIgA2 and B8-dIgA2 used in this study, neutralizing dIgA
500 belonging to other classes should also be investigated in future. We also do not know whether
501 other cellular receptor such as the polymeric immunoglobulin receptor (pIgR) plays a role in
502 B8-dIgA-enhanced SARS-CoV-2 nasal infection. The pIgR is responsible for transcytosis of
503 soluble dIgAs and immune complexes from the basolateral to the apical epithelial surface. It
504 remains uncertain whether B8-dIgA-enhanced NT infection would lead to worse neuro-
505 COVID-19. Because current intramuscular vaccinations might not induce secretory dIgA at
506 the nasal mucosal sites [74], it remains unknown whether the dIgA-mediated ADE would
507 happen in people who received the COVID-19 vaccines or dIgA treatment. Future studies are
508 needed to address these limitations.

509

510 **METHODS**
511 **Human subjects**
512 A total of 4 patients with COVID-19 including 3 convalescent cases and one acute case were
513 recruited between February and May 2020. All patients were confirmed by reverse-
514 transcription polymerase chain reaction (RT-PCR) as described previously [28]. Clinical and
515 laboratory findings were entered into a predesigned database. Written informed consent was
516 obtained from all patients. This study was approved by the Institutional Review Board of The
517 University of Hong Kong/Hospital Authority Hong Kong West Cluster, the Hong Kong East
518 Cluster Research Ethics Committee, and the Kowloon West Cluster Research Ethics
519 Committee (UW 13-265, HKECREC-2018-068, KW/EX-20-038[144-26]).

520

Syrian hamsters

The animal experimental plan was approved by the Committee on the Use of Live Animals in Teaching and Research (CULATR 5359-20) of the University of Hong Kong (HKU). Male and female golden Syrian hamsters (*Mesocricetus auratus*) (aged 6–10 weeks) were purchased from the Chinese University of Hong Kong Laboratory Animal Service Centre through the HKU Laboratory Animal Unit (LAU). The animals were kept in Biosafety Level-2 housing and given access to standard pellet feed and water ad libitum following LAU's standard operational procedures (SOPs). The viral challenge experiments were then conducted in our Biosafety Level-3 animal facility following SOPs strictly, with strict adherence to SOPs

Cell lines

HEK293T cells, HEK293T-hACE2 cells Vero-E6 cells, HK2 cells and Vero-E6-TMPRSS2 cells were maintained in DMEM containing 10% FBS, 2 mM L-glutamine, 100 U/mL/mL penicillin and incubated at 37 □ in a 5% CO_2 setting [62]. Expi293F^{TM} cells were cultured in Expi293TM Expression Medium (Thermo Fisher Scientific) at 37 □ in an incubator with 80% relative humidity and a 5% CO_2 setting on an orbital shaker platform at 125 ±5 rpm/min (New Brunswick innova™ 2100) according to the manufacturer's instructions.

ELISA analysis of plasma and antibody binding to RBD and trimeric spike

The recombinant RBD and trimeric spike proteins derived from SARS-CoV-2 (Sino Biological) were diluted to final concentrations of 1 μg/mL/mL, then coated onto 96-well plates (Corning 3690) and incubated at 4 °C overnight. Plates were washed with PBS-T (PBS containing 0.05% Tween-20) and blocked with blocking buffer (PBS containing 5% skim milk or 1% BSA) at 37 °C for 1 h. Serially diluted plasma samples or isolated monoclonal antibodies were added to the plates and incubated at 37 °C for 1 h. Wells were then incubated with a secondary goat anti-human IgG labelled with horseradish peroxidase (HRP) (Invitrogen) or with a rabbit polyclonal anti-human IgA alpha-chain labelled with HRP (Abcam) and TMB substrate (SIGMA). Optical density (OD) at 450 nm was measured by a spectrophotometer. Serially diluted plasma from healthy individuals or previously published monoclonal antibodies against HIV-1 (VRC01) were used as negative controls.

Isolation of RBD-specific IgG+ single memory B cells by FACS

554   RBD-specific single B cells were sorted as previously described [75]. In brief, PBMCs from

555   infected individuals were collected and incubated with an antibody cocktail and a His-tagged

556   RBD protein for identification of RBD-specific B cells. The cocktail consisted of the Zombie

557   viability dye (Biolegend), CD19-Percp-Cy5.5, CD3-Pacific Blue, CD14-Pacific Blue, CD56-

558   Pacific Blue, IgM-Pacific Blue, IgD- Pacific Blue , IgG-PE, CD27-PE-Cy7 (BD Biosciences)

559   and the recombinant RBD-His described above. Two consecutive staining steps were

560   conducted: the first one used an antibody and RBD cocktail incubation of 30 min at 4 °C; the

561   second staining involved staining with anti-His-APC and anti-His-FITC antibodies (Abcam)

562   at 4 °C for 30 min to detect the His tag of the RBD. The stained cells were washed and

563   resuspended in PBS containing 2% FBS before being strained through a 70-µm cell mesh

564   filter (BD Biosciences). RBD-specific single B cells were gated as $CD19^+CD27^+CD3^-CD14^-$

565   $CD56^-IgM^-IgD^-IgG^+RBD^+$ and sorted into 96-well PCR plates containing 10 µL of RNAase-

566   inhibiting RT-PCR catch buffer (1M Tris-HCl pH 8.0, RNase inhibitor, DEPC-treated water).

567   Plates were then snap-frozen on dry ice and stored at −80 °C until the reverse transcription

568   reaction.

569

570   **Single B cell RT-PCR and antibody cloning**

571   Single memory B cells isolated from PBMCs of infected patients were cloned as previously

572   described [76]. Briefly, one-step RT-PCR was performed on sorted single memory B cell with a

573   gene specific primer mix, followed by nested PCR amplifications and sequencing using the

574   heavy chain and light chain specific primers. Cloning PCR was then performed using heavy

575   chain and light chain specific primers containing specific restriction enzyme cutting sites

576   (heavy chain, 5′-AgeI/3′-SalI; kappa chain, 5′-AgeI/3′-BsiWI). The PCR products were

577   purified and cloned into the backbone of antibody expression vectors containing the constant

578   regions of human Igγ1 or Igα1 and Igα2. The Igα1 and Igα2 vectors were purchased from

579   InvivoGen (pfusess-hcha1 for IgA1 and pfusess-hcha2m1 for IgA2). The constructed

580   plasmids containing paired heavy and light chain expression cassettes were co-transfected

581   into 293T cells (ATCC) grown in 6-well plates. Antigen-specific ELISA and pseudovirus-

582   based neutralization assays were used to analyze the binding capacity to SARS-CoV-2 RBD

583   and the neutralization capacity of transfected culture supernatants, respectively.

584

585   **Genetic analysis of the BCR repertoire**

586   Heavy chain and light chain germline assignment, framework region annotation,

587   determination of somatic hypermutation (SHM) levels (in nucleotides) and CDR loop lengths

19

588   (in amino acids) were performed with the aid of the IMGT/HighV-QUEST software tool

589   suite (www.imgt.org/HighV-QUEST). Sequences were aligned using Clustal W in the

590   BioEdit sequence analysis package (Version 7.2). Antibody clonotypes were defined as a set

591   of sequences that share genetic V and J regions as well as an identical CDR3.

592

Antibody production and purification

594   The paired antibody VH/VL chains were cloned into Igγ, Igα1 or Igα2 and Ig*k* expression

595   vectors using T4 ligase (NEB). For production of IgG and monomeric IgA, the plasmids with

596   paired heavy chain (IgG, IgA1, IgA2) and light chain genes were co-transfected into

597   Expi293^{TM} expression system (Thermo Fisher Scientific) following the manufacturer's

598   protocol to produce recombinant monoclonal antibodies. For dIgA antibody production,

599   plasmids of paired heavy chain (IgA1, IgA2) and kappa light chain together with a J chain

600   were co-transfected into Expi293^{TM} expression system (Thermo Fisher Scientific) at the ratio

601   of 1:1:1 following the manufacturer's instructions. Antibodies produced from cell culture

602   supernatants were purified immediately by affinity chromatography using recombinant

603   Protein G-Agarose (Thermo Fisher Scientific) or CaptureSelect^{TM} IgA Affinity Matrix

604   (Thermo Fisher Scientific) according to the manufacturer's instructions, to purify IgG and

605   IgA, respectively. The purified antibodies were concentrated by an Amicon ultracentrifuge

606   filter device (molecular weight cut-off 10 kDa; Millipore) to a volume of 0.2 mL in PBS

607   (Life Technologies), and then stored at 4 °C or -80 °C for further characterization.

608

Size exclusion chromatography

610   The prepacked HiLoad 26/60 Superdex^{TM} 200pg (code No. 17-1071-01, Cytiva) column was

611   installed onto the Amersham Biosciences AKTA FPLC system. After column equilibration

612   with 2 column volumes (CV) of PBS, the concentrated IgA antibodies were applied onto the

613   column using a 500-ul loop at a flow rate of 2 mL/min. Dimers of IgA1 or IgA2 were

614   separated from monomers upon washing with 2 CV of PBS. The milli-absorbance unit at

615   OD280nm was recorded during the washing process. 2 mL-fractions were collected, pooled,

616   concentrated and evaluated by western blot using mouse anti-IGJ monoclonal antibody

617   [KT109] (Abcam) and rabbit anti-human IgA alpha chain antibody (Abcam).

618

Pseudovirus-based neutralization assay

620   The neutralizing activity of NAbs was determined using a pseudotype-based neutralization

621   assay as we previously described [77]. Briefly, The pseudovirus was generated by co-

622   transfection of 293T cells with pVax-1-S-COVID19 and pNL4-3Luc_Env_Vpr, carrying the

623   optimized spike (S) gene (QHR63250) and a human immunodeficiency virus type 1

624   backbone, respectively [77]. Viral supernatant was collected at 48 h post-transfection and frozen

625   at -80 °C until use. The serially diluted monoclonal antibodies or sera were incubated with

626   200 $TCID_{50}$ of pseudovirus at 37 °C for 1 hour. The antibody-virus mixtures were

627   subsequently added to pre-seeded HEK 293T-ACE2 cells. 48 hours later, infected cells were

628   lysed to measure luciferase activity using a commercial kit (Promega, Madison, WI). Half-

629   maximal (IC_{50}) or 90% (IC_{90}) inhibitory concentrations of the evaluated antibody were

630   determined by inhibitor vs. normalized response -- 4 Variable slope using GraphPad Prism 6

631   or later (GraphPad Software Inc.).

632

633   **Neutralization activity of monoclonal antibodies against authentic SARS-CoV-2**

634   The SARS-CoV-2 focus reduction neutralization test (FRNT) was performed in a certified

635   Biosafety level 3 laboratory. Neutralization assays against live SARS-CoV-2 were conducted

636   using a clinical isolate (HKU-001a strain, GenBank accession no: MT230904.1) previously

637   obtained from a nasopharyngeal swab from an infected patient [78]. The tested antibodies were

638   serially diluted, mixed with 50 μL of SARS-CoV-2 (1×10^3 focus forming unit/mL, FFU/mL)

639   in 96-well plates, and incubated for 1 hour at 37°C. Mixtures were then transferred to 96-well

640   plates pre-seeded with 1×10^4/well Vero E6 cells and incubated at 37°C for 24 hours. The

641   culture medium was then removed and the plates were air-dried in a biosafety cabinet (BSC)

642   for 20 mins. Cells were then fixed with a 4% paraformaldehyde solution for 30 min and air-

643   dried in the BSC again. Cells were further permeabilized with 0.2% Triton X-100 and

644   incubated with cross-reactive rabbit sera anti-SARS-CoV-2-N for 1 hour at RT before adding

645   an Alexa Fluor 488 goat anti-rabbit IgG (H+L) cross-adsorbed secondary antibody (Life

646   Technologies). The fluorescence density of SARS-CoV-2 infected cells were scanned using a

647   Sapphire Biomolecular Imager (Azure Biosystems) and the neutralization effects were then

648   quantified using Fiji software (NIH).

649

650   **Antibody binding kinetics, and competition with the ACE2 receptor measured by**

651   **Surface Plamon Resonance (SPR)**

652   The binding kinetics and affinity of recombinant monoclonal antibodies for the SARS-CoV-2

653   spike protein (ACROBiosystems) were analysed by SPR (Biacore 8K, GE Healthcare).

654   Specifically, the spike protein was covalently immobilized to a CM5 sensor chip via amine

655   groups in 10mM sodium acetate buffer (pH 5.0) for a final RU around 500. SPR assays were

656   run at a flow rate of 30 mL/min in HEPES buffer. For conventional kinetic/dose-response,

657   serial dilutions of monoclonal antibodies were injected across the spike protein surface for

658   180s, followed by a 600s dissociation phase using a multi-cycle method. Remaining analytes

659   were removed in the surface regeneration step with the injection of 10 mM glycine-HCl (pH

660   2.0) for 2×30s at a flow rate of 30 µl/min. Kinetic analysis of each reference subtracted

661   injection series was performed using the Biacore Insight Evaluation Software (GE

662   Healthcare). All sensorgram series were fit to a 1:1 (Langmuir) binding model of interaction.

663   Before evaluating the competition between antibodies and the human ACE2 peptidase

664   domain, both the saturating binding concentrations of antibodies and of the ACE2 protein

665   (ACROBiosystems) for the immobilized SARS-CoV-2 spike protein were determined

666   separately. In the competitive assay, antibodies at the saturating concentration were injected

667   onto the chip with immobilized spike protein for 120s until binding steady-state was reached.

668   ACE2 protein also used at the saturating concentration was then injected for 120s, followed

669   by another 120s of injection of antibody to ensure a saturation of the binding reaction against

670   the immobilized spike protein. The differences in response units between ACE2 injection

671   alone and prior antibody incubation reflect the antibodies' competitive ability against ACE2

672   binding to the spike protein.

673

674   **Hamster experiments**

675   *In vivo* evaluation of monoclonal antibody B8-IgG1, B8-mIgA1, B8-mIgA2, B8-dIgA1, B8-

676   dIgA2 in the established golden Syrian hamster model of SARS-CoV-2 infection was

677   performed as described previously, with slight modifications [48]. Approval was obtained from

678   the University of Hong Kong (HKU) Committee on the Use of Live Animals in Teaching and

679   Research. Briefly, 6-8-week-old male and female hamsters were housing with access to

680   standard pellet feed and water *ad libitum* until live virus challenge in the BSL-3 animal

681   facility. The hamsters were randomized from different litters into experimental groups.

682   Experiments were performed in compliance with the relevant ethical regulations [48]. For

683   prophylaxis studies, 24 hours before live virus challenge, three groups of hamsters were

684   intraperitoneally or intranasally administered with one dose of test antibody in phosphate-

685   buffered saline (PBS) at the indicated dose. At day 0, each hamster was intranasally

686   inoculated with a challenge dose of 100 μL of Dulbecco's Modified Eagle Medium

687   containing 10^5 PFU of SARS-CoV-2 (HKU-001a strain, GenBank accession no:

688   MT230904.1) under anaesthesia with intraperitoneal ketamine (200 mg/kg) and xylazine (10

689   mg/kg). For pre-treatment study, each hamster received one 1.5 mg/kg dose of intraperitoneal

22

690　B8-IgG1 at 24 , 48, 72 hours (n=4 per group) after virus challenge. The hamsters were

691　monitored twice daily for clinical signs of disease. Syrian hamsters typically clear virus

692　within one week after SARS-CoV-2 infection. Accordingly, animals were sacrificed for

693　analysis at day 4 after virus challenge with high viral loads [48]. Half the nasal turbinate,

694　trachea, and lung tissues were used for viral load determination by quantitative SARS-CoV-

695　2-specific RdRp/Hel RT-qPCR assay [28] and infectious virus titration by plaque assay [48].

696

Cryo-EM sample preparation and data acquisition

698　The purified SARS-CoV-2 S-B8 protein complexes were concentrated before being applied

699　to the grids. Aliquots (4 μL) of the protein complex were placed on glow-discharged holey

700　carbon grids (Quantifoil Au R1.2/1.3, 300 mesh). The grids were blotted and flash-frozen in

701　liquid ethane cooled by liquid nitrogen with a Vitrobot apparatus (Mark IV, ThermoFisher

702　Scientific). The grids sample quality was verified with an FEI Talos Arctica 200-kV electron

703　microscope (Thermo Fisher Scientific). The verified grids with optimal ice thickness and

704　particle density were transferred to a Titan Krios operating at 300 kV and equipped with a Cs

705　corrector, a Gatan K3 Summit detector (Gatan Inc.) and a GIF Quantum energy filter (slit

706　width 20 eV). Micrographs were recorded in the super-resolution mode with a calibrated

707　pixel size of 0.54895 Å. Each movie has a total accumulated exposure of 50 e−/Å2

708　fractionated in 32 frames. The final image was binned 2-fold to a pixel size of 1.0979 Å.

709　AutoEMation was used for the fully automated data collection. The defocus value of each

710　image, which was set from -1.0 to -2.0 μm during data collection, was determined by Gctf.

711　Data collection statistics are summarized in Supplementary Table 11.

712

Cryo-EM data processing

714　The procedure for image processing of SARS-CoV-2 S-B8 complex is presented in

715　Supplementary Fig. 2. In brief, Motion Correction (MotionCo2), CTF-estimation (GCTF) and

716　non-templated particle picking (Gautomatch, http://www.mrc-lmb.cam.ac.uk/kzhang/) were

717　automatically executed by the TsinghuaTitan.py program (developed by Dr. fang Yang).

718　Sequential data processing was carried out on RELION 3.0 and RELION 3.1. Initially,

719　2,436,776 particles were auto-picked by Gautomatch or RELION 3.0 from 4213 micrographs.

720　After several 2D classifications, 1,451,176 particles were selected and applied for 3D

721　classification with one class. Two different states were obtained after further 3D

722　classification: 3 RBD in up conformation bound with B8 Fab (3u), and 2 up RBDs and 1

723　down RBD with each bound to a B8 Fab (2u1d). 616,799 particles for the 2u1d state and

724 351,095 particles for the 3u state were subjected to 3D auto-refinement, yielding final

725 resolutions at 3.21 Å and 3.06 Å, respectively. Further CTF refinement and Bayesian

726 polishing improved the resolution to 2.65 Å (2u1d, C1 symmetry) and 2.67 Å (3u, C3

727 symmetry) with better map quality. To improve the RBD-B8 portion map density, focused

728 local search classification was applied for each RBD-B8 portion with an adapted soft mask.

729 The best classes for each RBD-Fab portion were selected and yielded a final resolution at

730 3.56 Å (RBD-Fab1, up), 3.34 Å (RBD-Fab2, up), 3.69 Å (RBD-Fab3, down), 3.87 Å (RBD-

731 Fab3, up) from 479,305, 508,653, 656,429, and 136,482 particles, respectively. Further CTF

732 refinement and Bayesian polishing improved the resolution of RBD-Fab2 to 3.11 Å with

733 better map quality. RBD-Fab maps were fitted onto the whole structure map using Chimera,

734 then combined using PHENIX combine_focused_maps. The reported resolutions were

735 estimated with the gold-standard Fourier shell correlation (FSC) cutoff of 0.143 criterion.

736 Data processing statistics are summarized in Supplementary Table 11.

737

738 **Model building and structure refinement**

739 The spike model (PDB code: 6VSB) and the initial model of the B8 Fab generated by

740 SWISS-Model were fitted into the EM density map, and further manually adjusted with Coot.

741 Glocusides were built manually with carbohydrate tool in Coot. The atomic models were

742 refinement using Phenix in real space with secondary structure and geometry restraints. The

743 final structures were validated using Phenix.molprobity. UCSF Chimera, ChimeraX and

744 PyMol were used for map segmentation and figure generation. Model refinement statistics

745 are summarized in Supplementary Table 11.

746

747 **SARS-CoV-2 infection of reconstructed human nasal epithelia**

748 MucilAir[TM], corresponding to reconstructed human nasal epithelium cultures differentiated *in*

749 *vitro* for at least 4 weeks, were purchased from Epithelix (Saint-Julien-en-Genevois, France).

750 The cultures were generated from pooled nasal tissues obtained from 14 human adult donors.

751 Cultures were maintained in air/liquid interface (ALI) conditions in transwells with 700 µL of

752 MucilAir[TM] medium (Epithelix) in the basal compartment, and then kept at 37 °C under a 5%

753 CO2 atmosphere. SARS-CoV-2 infection was performed as previously described [50]. Briefly,

754 the apical side of ALI cultures was washed 20 min at 37 °C in Mucilair[TM] medium to remove

755 mucus. Cells were then incubated with 10^4 plaque-forming units (PFU) of the isolate

756 BetaCoV/France/IDF00372/2020 (EVAg collection, Ref-SKU: 014V-03890; kindly provided

757 by S. Van der Werf). The viral input was diluted in DMEM medium to a final volume 100 µL,

758   and then left on the apical side for 4 h at 37 °C. Control wells were mock treated with

759   DMEM medium (Gibco) for the same duration. Viral inputs were removed by washing twice

760   with 200 µL of PBS (5 min at 37 °C) and once with 200 µL Mucilair^{TM} medium (20 min at

761   37 °C). The basal medium was replaced every 2-3 days. Apical supernatants were harvested

762   every 2-3 days by adding 200 µL of Mucilair^{TM} medium on the apical side, with an

763   incubation of 20 min at 37 °C prior to collection. For IgA treatment, cultures were washed

764   once and then pretreated with antibodies added to the apical compartment for 1 h in 50µL.

765   Viral input was then directly added to reach a final volume of 100 µL. The antibodies were

766   added again at day 2 d.p.i. in the apical compartment during an apical wash (20 min at 37 °C).

767   To test the effect of dIgA treatment in the presence of mucus, dIgA were added directly to the

768   apical compartment of MucilAir^{TM} cultures without an initial wash. After IgA treatment for

769   1h, the virus was added directly to the IgA/mucus mixture and left on the apical side for 4h at

770   37°C. After viral inoculation, a single brief wash was made to remove the viral input while

771   limiting mucus loss. The cultures were then maintained as in the no-mucus condition.

772

Viral RNA quantification in reconstructed human nasal epithelia

774   Apical supernatants were collected, stored at -80 °C until thawing and were then diluted 4-

775   fold in PBS in a 96-well plate. Diluted supernatants were inactivated for 20 min at 80 °C. For

776   SARS-CoV-2 RNA quantification, 1 µL of diluted supernatant was added to 4 µL of PCR

777   reaction mix. PCR was carried out in 384-well plates using the Luna Universal Probe One-

778   Step RT-qPCR Kit (New England Biolabs) with SARS-CoV-2 NP-specific primers (Forward

779   5'-TAA TCA GAC AAG GAA CTG ATT A-3'; Reverse 5'-CGA AGG TGT GAC TTC CAT

780   G-3') on a QuantStudio 6 Flex thermocycler (Applied Biosystems). A standard curve was

781   established in parallel using purified SARS-CoV-2 viral RNA.

782

Histopathology and immunofluorescence (IF) staining

784   The lung and nasal turbinate tissues collected at necropsy were fixed in zinc formalin and

785   then processed into paraffin-embedded tissue blocks. The tissue sections (4 µm) were stained

786   with hematoxylin and eosin (H&E) for light microscopy examination as previously described

787   with modifications [47]. For identification and localization of SARS-CoV-2 nucleocapsid

788   protein (NP) in organ tissues, immunofluorescence staining was performed on deparaffinized

789   and rehydrated tissue sections using a rabbit anti-SARS-CoV-2-NP protein antibody together

790   with an AF488-conjugated anti-rabbit IgG (Jackson ImmunoResearch, PA, USA). Briefly,

791   the tissue sections were first treated with antigen unmasking solution (Vector Laboratories) in

792   a pressure cooker. After blocking with 0.1% Sudan black B for 15 min and 1% bovine serum
793   albumin (BSA)/PBS at RT for 30 min, the primary rabbit anti-SARS-CoV-2-NP antibody
794   (1:4000 dilution with 1% BSA/PBS) was incubated at 4°C overnight. This step was followed
795   by incubation with a FITC-conjugated donkey anti-rabbit IgG (Jackson ImmunoResearch) for
796   30 min and the sections were then mounted in medium with 4',6-diamidino-2-phenylindole
797   (DAPI). For identification of DC-SIGN expression, we stained the NT slices with rabbit anti-
798   DC-SIGN primary antibody (Abcam) and Alexa Fluor 488 goat anti-rabbit IgG (H+L) cross-
799   adsorbed secondary antibody (Life Technologies) according to the manufacturer's
800   instructions. For identification of ACE2 expression, the goat anti-ACE2 primary antibody
801   (R&D) and Alexa Fluor 568 donkey anti-goat IgG (H+L) secondary antibodies (Invitrogen)
802   according to the manufacturer's instructions. All tissue sections were examined, and the
803   fluorescence images and whole section scanning were captured using 5×, 10× and 20×
804   objectives with Carl Zeiss LSM 980. NP$^+$ cells per field were quantified based on the mean
805   fluorescence intensity (MFI) using the ZEN BLACK 3.0 and ImageJ (NIH).

806

807   **Effects of B8-dIgA on SARS-CoV-2 infection in HK2 cells**
808   HK2 cells were seeded into 24-well plates at the 40-50% confluency and cultured overnight.
809   The B8-dIgA or control dIgA at the concentration of 1, 10, 100, 1000 ng/ml/mL and then
810   mixed with SARS-CoV-2 (1:10 TCID50) and incubated for 1 hour at room temperature. The
811   antibody/virus mixture was then added to HK2 cells after the cell culture medium was
812   removed and washed with PBS once and incubated for 1 hour at 37°C. The infectious
813   medium was replaced with fresh medium containing respective concentration of antibody
814   after washing 3 times with PBS. 24 h later, the infected cells were imaged under fluorescence
815   microscope after staining with AF488-conjugated anti-SARS-CoV-2 NP antibody.
816   Alternatively, the infected cells were lysed and blotted for SARS-CoV-2 NP protein to
817   determine the extent of infection. Tubulin was blotted as the internal control.

818

819   **B8-dIgA mediated enhancement via CD209**
820   HEK293T cells were seeded into 10-cm dish at 40% confluency and cultured overnight. The
821   HEK293T cells were transfected with human CD209 (Sino Biological) at 70%-90%
822   confluency. The expression of CD209 was measured by flow cytometry. The transfected
823   HEK293T-CD209 cells were seeded into 96-well plates with $2.4×10^4$ cells per well and
824   cultured overnight. The HEK293T-CD209 cells were pre-treated with 10 ng/ml/mL of B8-
825   dIgA or control dIgA and incubated for 6 h prior SARS-CoV-2 infection (MOI=0.05). 24 h

26

826   later, cells were then fixed with 4% paraformaldehyde solution for 30 min and air-dried in the

827   BSC. Cells were further permeabilized with 0.2% Triton X-100 and incubated with cross-

828   reactive rabbit sera anti-SARS-CoV-2-N for 1 hour at RT before adding Alexa Fluor 488 goat

829   anti-rabbit IgG (H+L) cross-adsorbed secondary antibody (Life Technologies). The

830   fluorescence density of SARS-CoV-2 infected cells was acquired using a Sapphire

831   Biomolecular Imager (Azure Biosystems) and then the MFI of four randomly selected areas

832   of each sample was quantified using Fiji software (NIH).

833

834   **Effects of B8 antibodies on SARS-CoV-2 mediated cell-cell fusion**

835   Vero-E6 TMPRSS2 cells were seeded into 48-well plates and cultured overnight. After

836   treatment with B8 antibodies at the dose of 3000 ng/ml/mL for 1 hour, HEK293T cells

837   transfected with SARS-CoV-2 spike-GFP were added into the treated Vero-E6 TMPRSS2

838   cells and co-cultured for 48 hours. The cell-cell fusion between Vero-E6 TMPRSS2 and

839   HEK293T-Spike-GFP was then determined under a fluorescence microscope (Nikon ELIPSE)

840   and the images of randomly selected region were captured using 4× and 10× objectives using

841   the Nikon software.

842

843   **Re-analysis of published nasal brushing single-cell data**

844   The preprocessed scRNA-seq data from nasal brushing samples of 2 healthy controls and 4

845   COVID-19 patients were downloaded from Gene Expression Omnibus (GEO) database with

846   accession numbers GSE171488 and GSE164547. Quality control metrics were consistent

847   with the original article [PMID: 34003804] and performed based on the R package Seurat

848   (version 4.0.3) [PMID: 34062119]. Harmony [PMID: 31740819] was used to integrate the

849   samples   based   on   the top   4000   most   variable genes   obtained with

850   the FindVariableFeatures() function in Seurat. CD14^{+} (monocyte) cells were extracted for

851   further analysis. The annotation of the cell type was performed by manually checking the

852   marker genes of each cluster identified from the FindAllMarkers() function in Seurat.

853

854   **Quantification and statistical analysis**

855   Statistical analysis was performed using PRISM 6.0 or later. Ordinary one-way ANOVA and

856   multiple comparisons were used to compare group means and differences between multiple

857   groups. Unpaired Student's *t* tests were used to compare group means between two groups

858   only. A P-value <0.05 was considered significant. The the number of independent

859   experiments performed, the number of animals in each group, and the specific details of

27

860   statistical tests are reported in the figure legends and the Methods section.

861

862   **SUPPLEMENTAL INFORMATION**

863   The supplemental information includes 13 Tables and 9 Figures.

864

865   **ACKNOWLEDGMENTS**

892

893   **AUTHOR CONTRIBUTIONS**

894 Conceptualization, Z.C.; HuNAb cloning, Z.B.; experimental design, Z.C., Z.B., R.Z.,

895 J.F.W.C.; hamster experiments, J.F.W.C., C.C.S.C., V.K.M.P., C.C.Y.C., K.K.H.C., and JC;

896 cryoEM study, J.Z., J.G., Z.Y.W., X.W.; SPR experiments, Q.Z., S.S. and L.Z.; LL confocal

897 imaging, L.L. and D.Z.; MucilAir^{TM} experiment, R.R. and L.A.C.; HK-2 experiment, M.L.Y.;

898 nasal cytology data analysis, M.Y. and R.S.; clinical specimens, K.K.W.T.; *in vitro*

899 experiments, H.C., Z.D., K.K.A., H.H., H.O.M., J.C., C.L., J.Z.; manuscript preparation,

900 Z.C., Z.B., R.Z., L.Z., K.Y.Y.; study supervision, Z.C., K.Y.Y. and L.Z.

901

902 **DECLARATION OF INTEREST**

903 J.F.W.C. has received travel grants from Pfizer Corporation Hong Kong and Astellas Pharma

904 Hong Kong Corporation Limited and was an invited speaker for Gilead Sciences Hong Kong

905 Limited and Luminex Corporation. The funding sources had no role in study design, data

906 collection, analysis or interpretation or writing of the report. The other authors declare no

907 conflicts of interest except for a provisional patent application filed for human monoclonal

908 antibodies generated in our laboratory.

909

910 **Reporting Summary**

911 Further information on research design is available in the Nature Research Reporting

912 Summary linked to this article.

913

914 **Data availability**

915 The data of this studies are available upon reasonable request and accession codes will be

916 available before publication.

917

918 **Code availability**

919 No custom computer code or algorithm used to generate results that are reported in the paper

920 and central to its main claims.

921

922 **REFERENCES**

923 1 Zhu, N. *et al.* A Novel Coronavirus from Patients with Pneumonia in China, 2019. *N*
924 *Engl J Med* **382**, 727-733, doi:10.1056/NEJMoa2001017 (2020).
925 2 Zhou, P. *et al.* A pneumonia outbreak associated with a new coronavirus of probable
926 bat origin. *Nature* **579**, 270-273, doi:10.1038/s41586-020-2012-7 (2020).
927 3 Wan, Y., Shang, J., Graham, R., Baric, R. S. & Li, F. Receptor recognition by novel
928 coronavirus from Wuhan: An analysis based on decade-long structural studies of
929 SARS. *J Virol* **94**, e00127-00120, doi:10.1128/JVI.00127-20 (2020).

930   4   Chan, J. F. *et al.* Genomic characterization of the 2019 novel human-pathogenic
931   coronavirus isolated from a patient with atypical pneumonia after visiting Wuhan.
932   *Emerg Microbes Infect* **9**, 221-236, doi:10.1080/22221751.2020.1719902 (2020).
933   5   Lu, G., Wang, Q. & Gao, G. F. Bat-to-human: spike features determining 'host jump'
934   of coronaviruses SARS-CoV, MERS-CoV, and beyond. *Trends Microbiol* **23**, 468-
935   478, doi:10.1016/j.tim.2015.06.003 (2015).
936   6   Shang, J. *et al.* Cell entry mechanisms of SARS-CoV-2. *Proc Natl Acad Sci U S A*
937   **117**, 11727-11734, doi:10.1073/pnas.2003138117 (2020).
938   7   Belouzard, S., Millet, J. K., Licitra, B. N. & Whittaker, G. R. Mechanisms of
939   coronavirus cell entry mediated by the viral spike protein. *Viruses* **4**, 1011-1033,
940   doi:10.3390/v4061011 (2012).
941   8   Wang, Q. *et al.* Structural and Functional Basis of SARS-CoV-2 Entry by Using
942   Human ACE2. *Cell* **181**, 894-904 e899, doi:10.1016/j.cell.2020.03.045 (2020).
943   9   Hoffmann, M. *et al.* SARS-CoV-2 Cell Entry Depends on ACE2 and TMPRSS2 and
944   Is Blocked by a Clinically Proven Protease Inhibitor. *Cell* **181**, 271-280 e278,
945   doi:10.1016/j.cell.2020.02.052 (2020).
946   10   Lan, J. *et al.* Structure of the SARS-CoV-2 spike receptor-binding domain bound to
947   the ACE2 receptor. *Nature* **581**, 215-220, doi:10.1038/s41586-020-2180-5 (2020).
948   11   Walls, A. C. *et al.* Structure, Function, and Antigenicity of the SARS-CoV-2 Spike
949   Glycoprotein. *Cell* **181**, 281-292 e286, doi:10.1016/j.cell.2020.02.058 (2020).
950   12   Yan, R. *et al.* Structural basis for the recognition of SARS-CoV-2 by full-length
951   human ACE2. *Science* **367**, 1444-1448, doi:10.1126/science.abb2762 (2020).
952   13   Lu, R. *et al.* Genomic characterisation and epidemiology of 2019 novel coronavirus:
953   implications for virus origins and receptor binding. *Lancet* **395**, 565-574,
954   doi:10.1016/S0140-6736(20)30251-8 (2020).
955   14   Wu, F. *et al.* A new coronavirus associated with human respiratory disease in China.
956   *Nature* **579**, 265-269, doi:10.1038/s41586-020-2008-3 (2020).
957   15   WHO. *Weekly epidemiological update on COVID-19 - 27 July 2021,*
958   *https://www.who.int/publications/m/item/weekly-epidemiological-update-on-covid-19-*
959   *--27-july-2021*, 2021).
960   16   Cheng, V. C., Lau, S. K., Woo, P. C. & Yuen, K. Y. Severe acute respiratory
961   syndrome coronavirus as an agent of emerging and reemerging infection. *Clin*
962   *Microbiol Rev* **20**, 660-694, doi:10.1128/CMR.00023-07 (2007).
963   17   Rothe, C. *et al.* Transmission of 2019-nCoV Infection from an Asymptomatic Contact
964   in Germany. *N Engl J Med* **382**, 970-971, doi:10.1056/NEJMc2001468 (2020).
965   18   Holshue, M. L. *et al.* First Case of 2019 Novel Coronavirus in the United States. *N*
966   *Engl J Med* **382**, 929-936, doi:10.1056/NEJMoa2001191 (2020).
967   19   Chan, J. F. *et al.* A familial cluster of pneumonia associated with the 2019 novel
968   coronavirus indicating person-to-person transmission: a study of a family cluster.
969   *Lancet* **395**, 514-523, doi:10.1016/S0140-6736(20)30154-9 (2020).
970   20   Wang, D. *et al.* Clinical Characteristics of 138 Hospitalized Patients With 2019 Novel
971   Coronavirus-Infected Pneumonia in Wuhan, China. *JAMA* **323**, 1061-1069,
972   doi:10.1001/jama.2020.1585 (2020).
973   21   Johnson, B. A. *et al.* Loss of furin cleavage site attenuates SARS-CoV-2 pathogenesis.
974   *Nature* **591**, 293-299, doi:10.1038/s41586-021-03237-4 (2021).
975   22   Wong, Y. C. *et al.* Natural transmission of bat-like SARS-CoV-2PRRA variants in
976   COVID-19 patients. *Clin Infect Dis* **73**, e437-e444, doi:10.1093/cid/ciaa953 (2020).
977   23   Chu, H. *et al.* Host and viral determinants for efficient SARS-CoV-2 infection of the
978   human lung. *Nat Commun* **12**, 134, doi:10.1038/s41467-020-20457-w (2021).

979   24   Gobeil, S. M. *et al.* D614G Mutation Alters SARS-CoV-2 Spike Conformation and
980   Enhances Protease Cleavage at the S1/S2 Junction. *Cell Rep* **34**, 108630,
981   doi:10.1016/j.celrep.2020.108630 (2021).
982   25   Korber, B. *et al.* Tracking Changes in SARS-CoV-2 Spike: Evidence that D614G
983   Increases Infectivity of the COVID-19 Virus. *Cell* **182**, 812-827 e819,
984   doi:10.1016/j.cell.2020.06.043 (2020).
985   26   Plante, J. A. *et al.* Spike mutation D614G alters SARS-CoV-2 fitness. *Nature* **592**,
986   116-121, doi:10.1038/s41586-020-2895-3 (2020).
987   27   Hung, I. F. *et al.* SARS-CoV-2 shedding and seroconversion among passengers
988   quarantined after disembarking a cruise ship: a case series. *Lancet Infect Dis* **20**,
989   1051-1060, doi:10.1016/S1473-3099(20)30364-9 (2020).
990   28   Chan, J. F. *et al.* Improved Molecular Diagnosis of COVID-19 by the Novel, Highly
991   Sensitive and Specific COVID-19-RdRp/Hel Real-Time Reverse Transcription-PCR
992   Assay Validated In Vitro and with Clinical Specimens. *J Clin Microbiol* **58**, e00310-
993   00320, doi:10.1128/JCM.00310-20 (2020).
994   29   To, K. K. *et al.* Temporal profiles of viral load in posterior oropharyngeal saliva
995   samples and serum antibody responses during infection by SARS-CoV-2: an
996   observational cohort study. *Lancet Infect Dis* **20**, 565-574, doi:10.1016/S1473-
997   3099(20)30196-1 (2020).
998   30   Arvin, A. M. *et al.* A perspective on potential antibody-dependent enhancement of
999   SARS-CoV-2. *Nature* **584**, 353-363, doi:10.1038/s41586-020-2538-8 (2020).
1000 31   Shi, R. *et al.* A human neutralizing antibody targets the receptor-binding site of
1001   SARS-CoV-2. *Nature* **584**, 120-124, doi:10.1038/s41586-020-2381-y (2020).
1002 32   Zost, S. J. *et al.* Potently neutralizing and protective human antibodies against SARS-
1003   CoV-2. *Nature* **584**, 443-449, doi:10.1038/s41586-020-2548-6 (2020).
1004 33   Liu, L. *et al.* Potent neutralizing antibodies against multiple epitopes on SARS-CoV-2
1005   spike. *Nature* **584**, 450-456, doi:10.1038/s41586-020-2571-7 (2020).
1006 34   Cao, Y. *et al.* Potent Neutralizing Antibodies against SARS-CoV-2 Identified by
1007   High-Throughput Single-Cell Sequencing of Convalescent Patients' B Cells. *Cell* **182**,
1008   73-84 e16, doi:10.1016/j.cell.2020.05.025 (2020).
1009 35   Robbiani, D. F. *et al.* Convergent antibody responses to SARS-CoV-2 in convalescent
1010   individuals. *Nature* **584**, 437-442, doi:10.1038/s41586-020-2456-9 (2020).
1011 36   Sun, Z. *et al.* Potent neutralization of SARS-CoV-2 by human antibody heavy-chain
1012   variable domains isolated from a large library with a new stable scaffold. *MAbs* **12**,
1013   1778435, doi:10.1080/19420862.2020.1778435 (2020).
1014 37   Wu, Y. *et al.* A noncompeting pair of human neutralizing antibodies block COVID-19
1015   virus binding to its receptor ACE2. *Science* **368**, 1274-1278,
1016   doi:10.1126/science.abc2241 (2020).
1017 38   Wu, Y. *et al.* Identification of Human Single-Domain Antibodies against SARS-CoV-
1018   2. *Cell Host Microbe* **27**, 891-898 e895, doi:10.1016/j.chom.2020.04.023 (2020).
1019 39   Pilette, C., Ouadrhiri, Y., Godding, V., Vaerman, J. P. & Sibille, Y. Lung mucosal
1020   immunity: immunoglobulin-A revisited. *Eur Respir J* **18**, 571-588,
1021   doi:10.1183/09031936.01.00228801 (2001).
1022 40   Corthesy, B. Multi-faceted functions of secretory IgA at mucosal surfaces. *Front
1023   Immunol* **4**, 185, doi:10.3389/fimmu.2013.00185 (2013).
1024 41   Ejemel, M. *et al.* A cross-reactive human IgA monoclonal antibody blocks SARS-
1025   CoV-2 spike-ACE2 interaction. *Nat Commun* **11**, 4198, doi:10.1038/s41467-020-
1026   18058-8 (2020).
1027 42   Sterlin, D. *et al.* IgA dominates the early neutralizing antibody response to SARS-
1028   CoV-2. *Sci Transl Med* **13**, eabd2223, doi:10.1126/scitranslmed.abd2223 (2021).

1029   43   Drummer, H. E. *et al.* Dimeric IgA is a specific biomarker of recent SARS-CoV-2
1030   infection. *medRxiv*, 2021.2006.2028.21259671, doi:10.1101/2021.06.28.21259671
1031   (2021).
1032   44   Dos Santos, J. M. B. *et al.* In Nasal Mucosal Secretions, Distinct IFN and IgA
1033   Responses Are Found in Severe and Mild SARS-CoV-2 Infection. *Front Immunol* **12**,
1034   595343, doi:10.3389/fimmu.2021.595343 (2021).
1035   45   Smith, N. *et al.* Distinct systemic and mucosal immune responses during acute SARS-
1036   CoV-2 infection. *Nat Immunol*, doi:10.1038/s41590-021-01028-7 (2021).
1037   46   Wang, Z. *et al.* Enhanced SARS-CoV-2 neutralization by dimeric IgA. *Sci Transl
1038   Med* **13**, eabf1555, doi:10.1126/scitranslmed.abf1555 (2021).
1039   47   Zhou, D. *et al.* Robust SARS-CoV-2 infection in nasal turbinates after treatment with
1040   systemic neutralizing antibodies. *Cell Host Microbe* **29**, 551-563,
1041   doi:10.1016/j.chom.2021.02.019 (2021).
1042   48   Chan, J. F.-W. *et al.* Simulation of the clinical and pathological manifestations of
1043   Coronavirus Disease 2019 (COVID-19) in golden Syrian hamster model: implications
1044   for disease pathogenesis and transmissibility. *Clinical Infectious Diseases* **71**, 2428-
1045   2446, doi:10.1093/cid/ciaa325 (2020).
1046   49   Yeung, M. L. *et al.* Soluble ACE2-mediated cell entry of SARS-CoV-2 via interaction
1047   with proteins related to the renin-angiotensin system. *Cell* **184**, 2212-2228 e2212,
1048   doi:10.1016/j.cell.2021.02.053 (2021).
1049   50   Robinot, R. *et al.* SARS-CoV-2 infection induces the dedifferentiation of multiciliated
1050   cells and impairs mucociliary clearance. *Nat Commun* **12**, 4354, doi:10.1038/s41467-
1051   021-24521-x (2021).
1052   51   Liu, L. *et al.* Spatiotemporal interplay of severe acute respiratory syndrome
1053   coronavirus and respiratory mucosal cells drives viral dissemination in rhesus
1054   macaques. *Mucosal Immunol* **9**, 1089-1101, doi:10.1038/mi.2015.127 (2016).
1055   52   Baumann, J., Park, C. G. & Mantis, N. J. Recognition of secretory IgA by DC-SIGN:
1056   implications for immune surveillance in the intestine. *Immunol Lett* **131**, 59-66,
1057   doi:10.1016/j.imlet.2010.03.005 (2010).
1058   53   Wang, R. *et al.* Analysis of SARS-CoV-2 variant mutations reveals neutralization
1059   escape mechanisms and the ability to use ACE2 receptors from additional species.
1060   *Immunity* **54**, 1611-1621 e1615, doi:10.1016/j.immuni.2021.06.003 (2021).
1061   54   Yang, L. *et al.* COVID-19 antibody therapeutics tracker: a global online database of
1062   antibody therapeutics for the prevention and treatment of COVID-19. *Antib Ther* **3**,
1063   205-212, doi:10.1093/abt/tbaa020 (2020).
1064   55   Watkins, J. D. *et al.* Anti-HIV IgA isotypes: differential virion capture and inhibition
1065   of transcytosis are linked to prevention of mucosal R5 SHIV transmission. *AIDS* **27**,
1066   F13-20, doi:10.1097/QAD.0b013e328360eac6 (2013).
1067   56   Merrill, W. W. *et al.* Free secretory component and other proteins in human lung
1068   lavage. *Am Rev Respir Dis* **122**, 156-161, doi:10.1164/arrd.1980.122.1.156 (1980).
1069   57   Taylor, R. A. *et al.* PET/CT targeted tissue sampling reveals virus specific dIgA can
1070   alter the distribution and localization of HIV after rectal exposure. *PLoS Pathog* **17**,
1071   e1009632, doi:10.1371/journal.ppat.1009632 (2021).
1072   58   Beltramello, M. *et al.* The Human Immune Response to Dengue Virus Is Dominated
1073   by Highly Cross-Reactive Antibodies Endowed with Neutralizing and Enhancing
1074   Activity. *Cell Host & Microbe* **8**, 271-283, doi:10.1016/j.chom.2010.08.007 (2010).
1075   59   Bournazos, S. *et al.* Antibody fucosylation predicts disease severity in secondary
1076   dengue infection. *Science* **372**, 1102-1105, doi:10.1126/science.abc7303 (2021).

1077 60 van Erp, E. A., Luytjes, W., Ferwerda, G. & van Kasteren, P. B. Fc-Mediated
1078 Antibody Effector Functions During Respiratory Syncytial Virus Infection and
1079 Disease. *Front Immunol* **10**, 548, doi:10.3389/fimmu.2019.00548 (2019).
1080 61 Wan, Y. *et al.* Molecular Mechanism for Antibody-Dependent Enhancement of
1081 Coronavirus Entry. *J Virol* **94**, e02015-02019, doi:10.1128/JVI.02015-19 (2020).
1082 62 Liu, L. *et al.* Anti-spike IgG causes severe acute lung injury by skewing macrophage
1083 responses during acute SARS-CoV infection. *JCI Insight* **4**, e123158,
1084 doi:10.1172/jci.insight.123158 (2019).
1085 63 Haynes, B. F. *et al.* Prospects for a safe COVID-19 vaccine. *Sci Transl Med* **12**,
1086 doi:10.1126/scitranslmed.abe0948 (2020).
1087 64 Larsen, M. D. *et al.* Afucosylated IgG characterizes enveloped viral responses and
1088 correlates with COVID-19 severity. *Science* **371**, doi:10.1126/science.abc8378 (2021).
1089 65 Baum, A. *et al.* REGN-COV2 antibodies prevent and treat SARS-CoV-2 infection in
1090 rhesus macaques and hamsters. *Science* **370**, 1110-1115, doi:10.1126/science.abe2402
1091 (2020).
1092 66 Liu, Y. *et al.* An infectivity-enhancing site on the SARS-CoV-2 spike protein targeted
1093 by antibodies. *Cell* **184**, 3452-3466 e3418, doi:10.1016/j.cell.2021.05.032 (2021).
1094 67 Soh, W. T. *et al.* The N-terminal domain of spike glycoprotein mediates SARS-CoV-
1095 2 infection by associating with L-SIGN and DC-SIGN. *bioRxiv*,
1096 2020.2011.2005.369264, doi:10.1101/2020.11.05.369264 (2020).
1097 68 Geijtenbeek, T. B. H. *et al.* DC-SIGN, a dendritic cell-specific HIV-1-binding protein
1098 that enhances trans-infection of T cells. *Cell* **100**, 587-597, doi:Doi 10.1016/S0092-
1099 8674(00)80694-7 (2000).
1100 69 Bracq, L., Xie, M., Benichou, S. & Bouchet, J. Mechanisms for Cell-to-Cell
1101 Transmission of HIV-1. *Front Immunol* **9**, 260, doi:10.3389/fimmu.2018.00260
1102 (2018).
1103 70 Yang, D. *et al.* Attenuated Interferon and Proinflammatory Response in SARS-CoV-
1104 2-Infected Human Dendritic Cells Is Associated With Viral Antagonism of STAT1
1105 Phosphorylation. *J Infect Dis* **222**, 734-745, doi:10.1093/infdis/jiaa356 (2020).
1106 71 Thepaut, M. *et al.* DC/L-SIGN recognition of spike glycoprotein promotes SARS-
1107 CoV-2 trans-infection and can be inhibited by a glycomimetic antagonist. *PLoS*
1108 *Pathog* **17**, e1009576, doi:10.1371/journal.ppat.1009576 (2021).
1109 72 Hartmann, E. *et al.* Analysis of plasmacytoid and myeloid dendritic cells in nasal
1110 epithelium. *Clin Vaccine Immunol* **13**, 1278-1286, doi:10.1128/CVI.00172-06 (2006).
1111 73 Ahn, J. H. *et al.* Nasal ciliated cells are primary targets for SARS-CoV-2 replication
1112 in the early stage of COVID-19. *J Clin Invest* **131**, e148517, doi:10.1172/JCI148517
1113 (2021).
1114 74 Krammer, F. SARS-CoV-2 vaccines in development. *Nature* **586**, 516-527,
1115 doi:10.1038/s41586-020-2798-3 (2020).
1116 75 Kong, L. *et al.* Key gp120 Glycans Pose Roadblocks to the Rapid Development of
1117 VRC01-Class Antibodies in an HIV-1-Infected Chinese Donor. *Immunity* **44**, 939-950,
1118 doi:10.1016/j.immuni.2016.03.006 (2016).
1119 76 Smith, K. *et al.* Rapid generation of fully human monoclonal antibodies specific to a
1120 vaccinating antigen. *Nat Protoc* **4**, 372-384, doi:10.1038/nprot.2009.3 (2009).
1121 77 Poeran, J., Zhong, H., Wilson, L., Liu, J. & Memtsoudis, S. G. Cancellation of
1122 elective surgery and intensive care unit capacity in New York state: a retrospective
1123 cohort analysis. *Anesth Analg* **131**, 1337-1341, doi:10.1213/ANE.0000000000005083
1124 (2020).
1125 78 Chu, H. *et al.* Comparative tropism, replication kinetics, and cell damage profiling of
1126 SARS-CoV-2 and SARS-CoV with implications for clinical manifestations,

1127   transmissibility, and laboratory studies of COVID-19: an observational study. *The*

1128   *Lancet Microbe* **1**, e14-e23, doi:10.1016/S2666-5247(20)30004-5 (2020).

1129

1130   **FIGURE LEGENDS**

1131

1132   **Fig. 1. Isolation of monoclonal antibodies from single B cells of convalescent COVID-19**

1133   **patients.**

1134   **(A)** RBD-specific binding activities of sera derived from 3 (P1-P3) convalescent and 1 (P4)

1135   acute COVID-19 patients as measured by ELISA.

1136   **(B)** Spike-specific binding activities of sera derived from four COVID-19 patients as

1137   measured by ELISA.

1138   **(C)** Neutralization activities of sera derived from four COVID-19 patients as measured by

1139   pseudotyped SARS-CoV-2 inhibition in 293T-ACE2 cells.

1140   **(D)** Antibody gene repertoire analysis of reactive B cells derived from each patient. The

1141   number of cloned antibody genes from each patient is shown in the center of each pie chart

1142   for both the heavy (H) and light (L) chains. The colors represent specific variable gene family.

1143   Each fragment of the same color stands for one specific sub-family.

1144   **(E)**. The percentage of somatic hypermutation (SHM) compared to germline sequences and

1145   the CDR3 amino acid lengths of cloned antibody H and L gene sequences were analyzed for

1146   each subject.

1147   **(F)** RBD (left) and spike (right) specific binding activities of five HuNAbs, including A6, B4,

1148   B7, B8 and C5, were measured by ELISA.

1149   **(G)** Neutralization activities of 5 HuNAbs against pseudotyped (left) and authentic (right)

1150   SARS-CoV-2 were determined in HEK 293T-ACE2 and Vero-E6 cells, respectively. HIV-1

1151   specific HuNAb VRC01 served as a negative control. Each assay was performed in

1152   duplicates and the mean of replicates is shown with the standard error of mean (SEM).

1153   **(H)** The competition of four HuNAbs, including B4, B7, B8 and C5, with human soluble

1154   ACE2 for binding to SARS-CoV-2 RBD was measured by SPR. The curves show binding of

1155   ACE2 to SARS-CoV-2 RBD with (red) or without (black) pre-incubation with each HuNAb.

1156

1157   **Fig. 2. Pre- and post-exposure treatment of B8-IgG1 against SARS-CoV-2 in Syrian**

1158   **Hamster.**

1159 **(A)** Experimental schedule. Four groups of hamsters (G1-G4) received intraperitoneally a

1160 single dose of 1.5 mg/kg of B8-IgG1 at one day before infection (-1 dpi) for pre-exposure

1161 prophylaxis, and at day one (1 dpi), two (2 dpi) and three (3 dpi) post-infection for early

1162 treatment, respectively.

1163 Control hamsters (G0, n=4) received an isotypic control antibody at the same dose. On day 0,

1164 each hamster was intranasally challenged with a dose of 10^5 PFU of SARS-CoV-2 (HKU-

1165 001a strain). All hamsters were sacrificed on 4 dpi for analysis.

1166 **(B)** Infectious virus (PFU) was measured in animal lungs by the viral plaque assay in Vero-

1167 E6 cells. The PFU/ml concentration is shown in log-transformed units.

1168 **(C)** The relative viral RdRp RNA copies (normalized to β-actin) were determined by RT-

1169 PCR in animal lungs.

1170 **(D)** Representative 100× images of infected lungs from each group, as determined by anti-NP

1171 immunofluorescence (IF) staining. The cell nuclei were counterstained with DAPI (blue).

1172 **(E)** Infectious virus (PFU) were measured in NT homogenates by the viral plaque assay as

1173 mentioned above.

1174 **(F)** Viral loads in NT homogenates of each group were determined by RT-PCR assay. The

1175 viral load data is shown in log-transformed units.

1176 **(G)** Representative 100× images of infected NT from each group as determined by anti-NP IF

1177 staining as mentioned above.

1178 Statistics were generated using one-way ANOVA tests. *$p<0.05$; **$p<0.01$; ***$p<0.001$.

1179

1180 **Fig. 3. Pre-exposure treatment with monomeric B8-mIgA1 or B8-mIgA2 against SARS-**

1181 **CoV-2 infection in Syrian hamsters.**

1182 **(A)** Experimental schedule. Five groups of hamsters (n=4 per group) received a single dose

1183 of 4.5 mg/kg of B8-IgG1, B8-mIgA1 or B8-mIgA2 one day before viral challenge for pre-

1184 exposure prophylaxis by the intranasal route (circles) or the intraperitoneal route (triangles),

1185 respectively. Control hamsters (n=4) received PBS. On day 0, each hamster was intranasally

1186 challenged with a dose of 10^5 PFU of SARS-CoV-2, as mentioned in Fig. 2A. All hamsters

1187 were sacrificed on 4 dpi for analysis.

1188 **(B)** The viral RNA load, measured by relative RdRp RNA copy numbers (normalized to β-

1189 actin) was determined by RT-PCR in animal lung homogenates.

1190 **(C)** The relative sub-genomic nucleocapsid (sgNP) RNA copy numbers (normalized to β-

1191 actin) were determined by RT-PCR in animal lung homogenates.

1192 **(D)** Infectious virus (PFU) was measured in animal lung homogenates by the viral plaque

1193 assay in Vero-E6 cells.

1194 **(E)** Representative lung images of infected animals by scanning whole tissue section. The

1195 signal of SARS-CoV-2 NP was shown in bright spots.

1196 **(F)** The relative viral RdRp RNA copy numbers (normalized to β-actin) were determined by

1197 RT-PCR in NT homogenates.

1198 **(G)** The relative sgNP RNA copy numbers (normalized to β-actin) were determined by RT-

1199 PCR in NT homogenates.

1200 **(H)** Infectious virus (PFU) was measured in animal NT homogenates by the viral plaque

1201 assay in Vero-E6 cells.

1202 **(I)** Representative NT images of infected animals by scanning whole tissue section. The

1203 signal of SARS-CoV-2 NP was shown in bright spots.

1204 Log-transformed units are shown in **(B) to (H)** except in **(E)**. Statistics were generated using

1205 one-way ANOVA tests. *$p < 0.05$; **$p < 0.01$.

1206

1207 **Fig. 4. Pre-exposure treatment with dimeric B8-dIgA enhances SARS-CoV-2 infection**

1208 **in Syrian hamsters.**

1209 **(A)** Experimental schedule. Four groups of hamsters (n=4 per group) were inoculated

1210 intranasally with B8-dIgA1 or B8-dIgA2, either at a low dose of 4.5 mg/kg or at a high dose

1211 of 13.5 mg/kg, respectively, 12 hours before intranasal viral challenge. Another group of

1212 hamsters (n=4) received PBS as control. On day 0, each hamster was intranasally challenged

1213 with a dose of 10^5 PFU of SARS-CoV-2 as described in Fig. 2A. All hamsters were

1214 sacrificed on 4 dpi for analysis. Data represent a presentative experiment from three

1215 independent experiments.

1216 **(B)** The relative viral RdRp RNA copy numbers (normalized to β-actin) were determined by

1217 RT-PCR in animal lung homogenates.

1218 **(C)** The relative viral sgNP RNA copy numbers (normalized to β-actin) were determined by

1219 RT-PCR in animal lung homogenates.

1220 **(D)** Infectious virus (PFU) was measured in animal lung homogenates by the viral plaque

1221 assay in Vero-E6 cells.

1222 **(E)** Representative lung images of infected animals by scanning whole tissue section. The

1223 signal of SARS-CoV-2 NP was shown in bright spots.

1224   **(F)** The relative viral RdRp RNA copy numbers (normalized to β-actin) were determined by

1225   RT-PCR in NT homogenates.

1226   **(G)** The relative viral sgNP RNA copies (normalized to β-actin) were determined by RT-

1227   PCR in NT homogenates.

1228   **(H)** Infectious virus (PFU) was measured in NT homogenates by the viral plaque assay in

1229   Vero-E6 cells.

1230   **(I)** Representative NT images of infected animals by scanning whole tissue section. The

1231   signal of SARS-CoV-2 NP was shown in bright spots.

1232   Log-transformed units are shown in **(B) to (H)** except in **(E)**. Statistics were generated using

1233   one-way ANOVA tests. $*p<0.05$; $**p<0.01$.

1234

1235   **Fig. 5. B8-dIgA1 and B8-dIgA2 enhance SARS-CoV-2 infection via CD209.**

1236   **(A)** The effects of B8-dIgA2 on SARS-CoV-2 infection in the MucilAir™ model, consisting

1237   of primary human nasal epithelial cells but no DCs. B8-mIgA2 or B8-dIgA2 were pre-

1238   incubated at doses of 10, 100, and 1000 ng/ml, respectively, in the apical compartment with

1239   or without mucus for 1 hour, before adding 10^4 PFU of SARS-CoV-2

1240   (BetaCoV/France/IDF00372/2020) for 4 hours. The viral RNA loads were measured by RT-

1241   PCR in both the apical and basal compartments and are shown in log-transformed units.

1242   **(B)** Representative confocal images (400×) of olfactory epithelium in NT showed the

1243   expression of CD209 (DC-SIGN) in green and ACE2 in magenta by immunohistochemical

1244   staining of experimental hamsters treated with B8-dIgA2 without (left) or with (middle and

1245   right) SARS-CoV-2 infection. Color-coding indicates specific antibodies used for double

1246   staining. Infected CD209$^+$ cells are visualized in yellow as indicated by arrows (right).

1247   **(C)** The CD209 or CD299 overexpressed-HEK 293T cells were pre-treated for 6 hours with

1248   10 ng/ml of B8-dIgA1 or B8-dIgA2 or control dIgA1 or control dIgA2 or PBS, respectively,

1249   prior to SARS-CoV-2 infection (MOI: 0.05). Two days after infection, SARS-CoV-2 NP

1250   expression (green) was quantified by the mean fluorescence intensity (MFI) after anti-NP IF

1251   staining. Statistics were generated using student-*t* tests. $*p<0.05$; $**p<0.01$; $***p<0.001$.

1252   **(D)** The effects of B8 antibodies on cell-cell fusion. 293T cells co-transfected with SARS-

1253   CoV-2 spike and GFP were pre-treated with 100× the IC$_{90}$ dose of B8-IgG1, B8-mIgA1, B8-

1254   mIgA2, B8-dIgA1, B8-dIgA2 or and IgG isotypic control for 1 hour, respectively. Vero-E6

1255   cells transfected with TMPRSS2 were then added to the treated 293T-spike-GFP cells and

37

1256   co-cultured for 48 hours.   Cell-cell fusion was imaged under a fluorescence confocal

1257   microscope at the 50× magnification.

1258

1259   **Fig. 6. Cryo-EM structures of the SARS-CoV-2 S trimer in complex with B8-Fabs.**

1260   (**A**) Side and top views of the Spike-B8 3u cryo-EM map showing 3 up RBDs each bound

1261   with a B8 Fab. Protomer 1, 2, and 3 are shown in slate blue, dark sea green, and India red,

1262   respectively. Heavy chain and light chain of the B8-Fab are in blue and gold, respectively.

1263   This color scheme was used throughout panels (**A**)-(**E**).

1264   (**B**) Side and top views of the Spike-B8 3u cryo atomic model.

1265   (**C**) Side and top views of the Spike-B8 2u1d cryo-EM map showing two up RBDs up (RBD-

1266   1 and RBD-2) and one RBD down (RBD-3), each bound to a B8-Fab.

1267   (**D**) Side and top views of the Spike-B8 2u1d cryo atomic model.

1268   (**E**) Structural comparation of RBDs between Spike-B8 3u (different colors) and Spike-B8

1269   2u1d (gray).

1270   (**F**) ACE2 (chocolate color, PDB: 6M0J) may clash with the heavy chain (blue) and light

1271   chain (gold) of the B8-Fab. ACE2 and the Fab share overlapping epitopes on the RBM

1272   (dotted black circle), and the framework of the B8-VL appears to clash with ACE2 (dotted

1273   black frame). The RBD core and RBM are shown in light sky blue and green, respectively.

1274   (**G**) Atomic model of an RBD-B8 complex portion in cartoon mode, shown with the same

1275   color scheme as in (**F**).

1276   (**H**) The residues involved in interactions between B8 and the RBM. The heavy and light

1277   chain of the B8-Fab are in blue and gold, respectively. The RBM is shown in green.
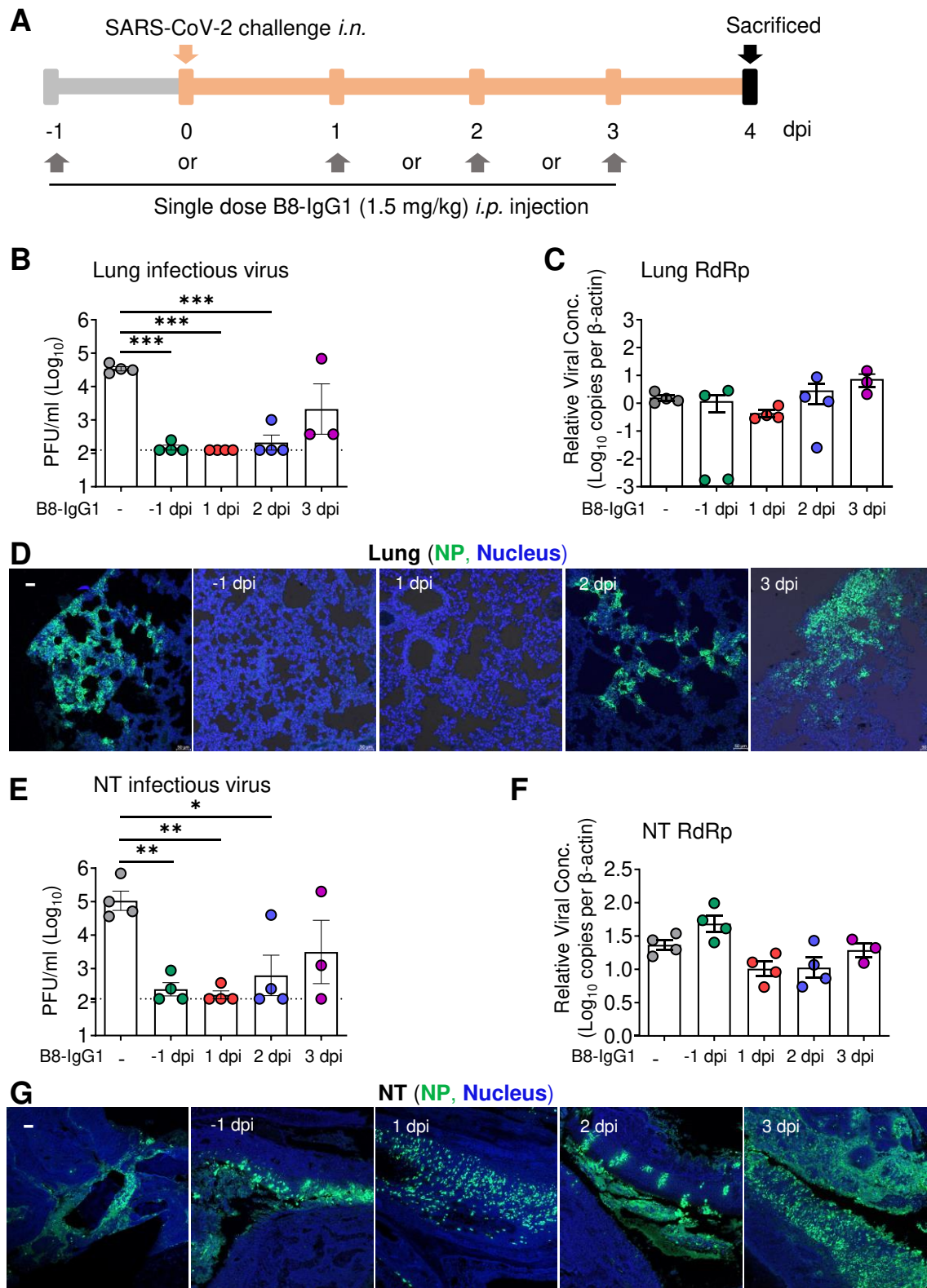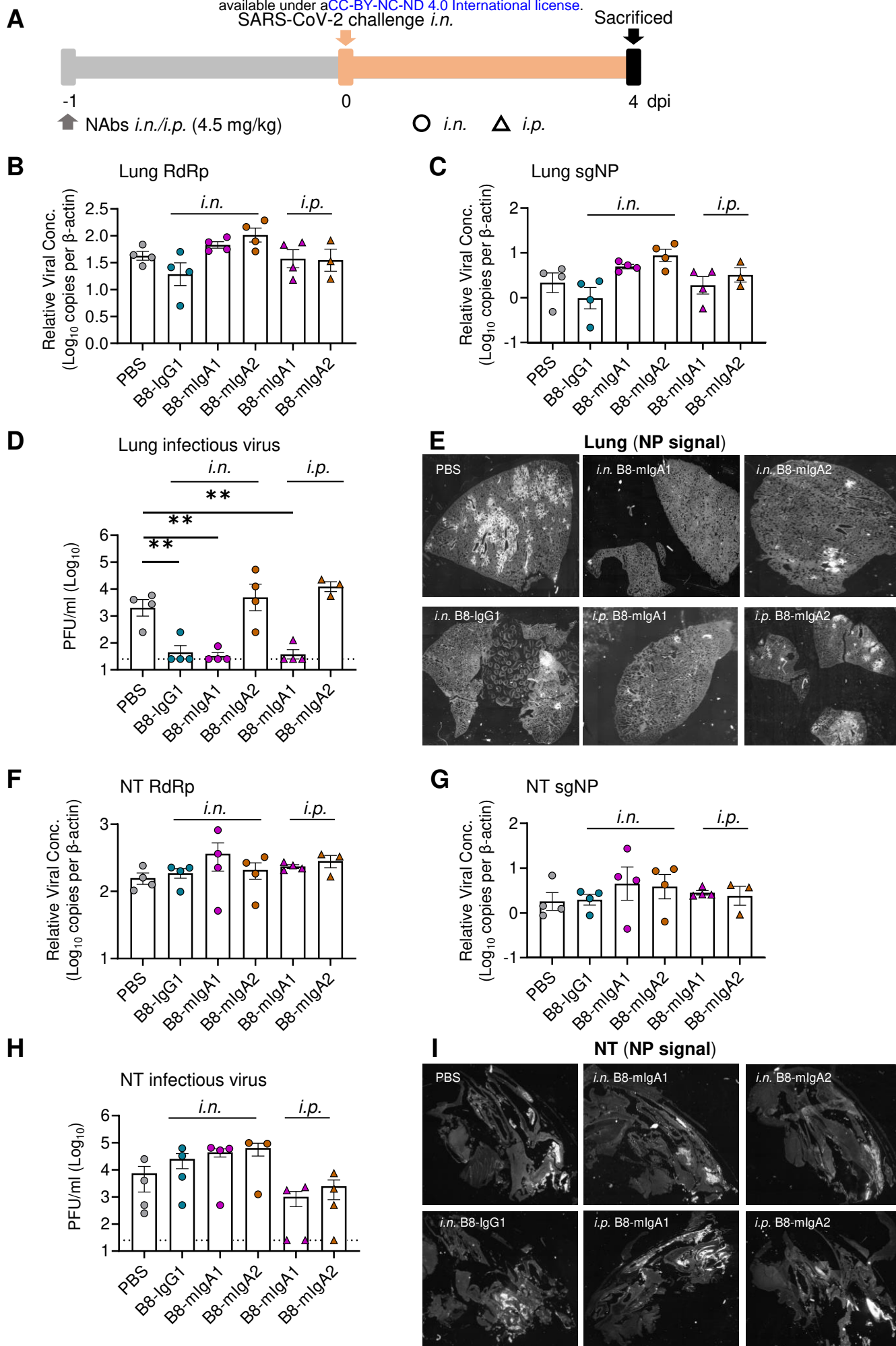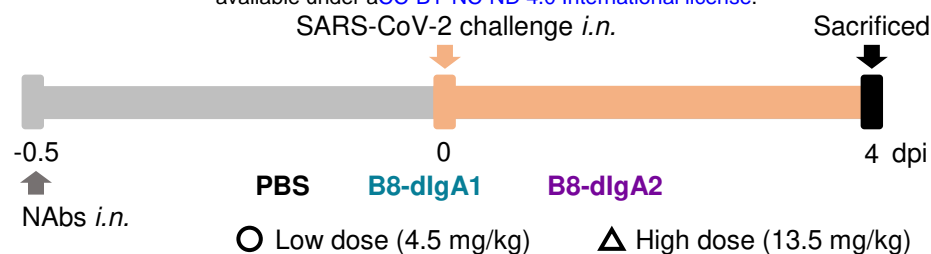
Fig. 1

Fig. 2

Fig. 3

Fig. 4

A

SARS-CoV-2 challenge *i.n.* Sacrificed

-0.5   0   4 dpi

NAbs *i.n.*

PBS   **B8-dIgA1**   **B8-dIgA2**

○ Low dose (4.5 mg/kg)   △ High dose (13.5 mg/kg)

B   Lung RdRp

C   Lung sgNP

D   Lung infectious virus

E   **Lung (NP signal)**

F   NT RdRp

G   NT sgNP

H   NT infectious virus

I   **NT (NP signal)**

Fig. 5

Fig. 6